Distribution and Valence State of Ru Species on CeO_2 Supports: Support Shape Effect and Its Influence on CO Oxidation

Junhao Li,[1] Zhongqi Liu,[1] David A. Cullen,[2]* Wenhui Hu,[3] Jier Huang,[3] Libo Yao,[4] Zhenmeng Peng,[4] Peilin Liao,[5] and Ruigang Wang[1]*

[1]*Department of Metallurgical and Materials Engineering, The University of Alabama, Tuscaloosa, AL 35487, United States*

[2]*Center for Nanophase Materials Sciences, Oak Ridge National Laboratory, Oak Ridge, TN 37831, United States*

[3]*Department of Chemistry, Marquette University, Milwaukee, WI 53201, United States*

[4]*Department of Chemical and Biomolecular Engineering, The University of Akron, Akron, OH 44325, United States*

[5]*School of Materials Engineering, Purdue University, West Lafayette, IN 47907, United States*

***Corresponding authors: rwang@eng.ua.edu (R. Wang); cullenda@ornl.gov (D.A. Cullen)**

Abstract

In this work, ruthenium (Ru) catalysts supported on CeO_2 nanorods (NR), nanocubes (NC) and nanoctahedra (NO) were comparatively investigated to correlate the shape and exposed surface planes ({100}, {110}, and {111}) of nanoscale CeO_2 supports with their low-temperature CO oxidation activity. Within the 5Ru/CeO_2-r catalysts with three morphologies after reduction treatment, the Ru supported on CeO_2 NR exhibited enhanced low-temperature (< 100 °C) hydrogen consumption and superior room-temperature CO oxidation activity (~9% CO conversion). Both

X-ray photoelectron spectroscopy (XPS) and X-ray absorption spectroscopy (XAS) measurements revealed that Ru^{n+} homogeneously predominates the 5Ru/CeO_2NR-r, which is very different from partial metallic Ru^0 supported on CeO_2 NC and NO, indicating the strong metal-support interaction formation between Ru and CeO_2 NR by Ru ions diffusing into CeO_2 surface lattice or forming Ru-O-Ce bonds at the interface. The enriched surface defects on the exposed {111} planes of CeO_2 NR support are believed to be the key to the formation of cationic Ru species, which is of vital importance for the superior room-temperature CO oxidation activity of 5Ru/CeO_2NR-r catalyst. The higher surface oxygen vacancy concentration on the 5Ru/CeO_2NR-r than those on the CeO_2 NC and NO are also crucial for adsorption/dissociation of oxygen in achieving low-temperature CO oxidation activity.

Keywords: RuO_x/CeO_2 catalyst; morphology effects; reduction treatment; oxygen storage capacity; CO oxidation

1. Introduction

Ceria (CeO_2), as a catalyst, a catalyst support, or even a simple mysterious constituent, has gained significant attention in various fundamental science and application fields such as heterogeneous catalysis, solid oxide fuel cells, and oxygen sensors as well as biotechnology, environmental chemistry and medicine [1-6]. It is widely exploited to support transition or noble metal catalysts, enabling improved dispersion, thermal stability, and catalytic properties in CO/soot/VOC oxidation [7-9], WGS reaction [10], hydrogenation [11], partial oxidation of CH_4 to synthesis gas [12], and so on. The unique contribution of CeO_2 in these applications relies on its high oxygen storage capacity (OSC) and oxygen mobility, deriving from facile switching

between the Ce^{4+} and Ce^{3+} chemical states through forming and eliminating oxygen vacancies at the different CeO_2 surfaces ({100}, {110}, and {111}) [13, 14].

Considerable research efforts in the past decade have been dedicated to preparing specific morphologies of CeO_2 such as nanoctahedra (NO), nanocubes (NC), nanorods (NR), nanowires (NW), and nanospheres (NS) and clarifying the morphology/facet-dependent catalytic activity of CeO_2 nanomaterials [15-17]. In comparison with thermally stable octahedral CeO_2 nanoparticles, the tuned morphologies of CeO_2 like rods or cubes which expose specific facets can considerably improve many redox-related catalytic performances [18-20]. The three most thermodynamically stable surfaces for CeO_2 are {111}, {110} and {100} facets with different coordination numbers [20]. The surface energy values of the three facets are in the following sequence: {111} < {110} < {100} [21]. As for the oxygen vacancy (defect) formation energy, the order is {110} < {100} < {111} [22]. It is well accepted that the most stable facet {111} is preferentially present on CeO_2 NO, while {100} facet is exposed by CeO_2 NC. However, there is still a controversy over the type of exposed facets on CeO_2 NR. Generally, CeO_2 NR has been reported to be enclosed by two {100} and two {110} facets and grow along the [110] direction [15, 23]. Recently, detailed high-resolution transmission electron microscopy (TEM) investigations [24, 25] show that CeO_2 NR can also expose {111} facets with a large number of surface defects, including steps, voids, and so on. Ta et al. [26] reported that gold particles of 2-4 nm size, strongly anchored onto the {111} facets of CeO_2 NR, are highly active as well as peculiarly stable even under realistic reaction conditions. Wang et al. [25] attributed the robust low-temperature CO oxidation activity of CeO_2 NR supported transition metal catalysts not only to the support shape but also to the defected {111} surface.

In CeO_2-supported noble metal heterogeneous catalysts, it has been acknowledged that the metal-oxide interaction/reaction at the interface can greatly affect the nature of the noble metal (e.g. dispersion, size distribution, valence state, and thermal stability), and hence their catalytic properties. At the same time, these strong metal-support interactions also contribute to noble metal atoms/clusters trapping or bonding onto the support surface, charge transferring and mass transporting (diffusion) between catalyst and support, and defects and strain creating at the interface during catalysts preparation and posttreatment under oxidizing or reducing conditions. It was reported by Satsuma et al. [27] that self-dispersion of large-sized Ru particles into nanoparticles was caused by forming Ru-O-Ce bond during oxidation of Ru metal into Ru oxide in air. Aitbekova et al. [28] also found that oxidation treatment causes redispersion of Ru nanoparticles supported on CeO_2, generating stable RuO_x/CeO_2 species strongly bonded to the CeO_2 support which shows remarkable selectivity for CO production. Guo et al. [29] contributed the average Ru valence decreasing from +4.1 for Ru(single atom)/CeO_2 to +3.7 for Ru(nanoparticle)/CeO_2 on reduction by H_2 to a weakened electronic interaction from Ru single atoms to nanoparticles at the interface. The investigation results of Slavinskaya et al. [30] showed that the superior low-temperature CO oxidation activity (T_{10} = 17 °C) of the Pd/CeO_2 catalyst was determined by two cationic palladium species: the surface $Pd_xCe_{1-x}O_{2-\delta}$ solid solution phase and surface PdO_x/Pd-O-Ce composite structure, which are formed owing to the strong interaction between the palladium species and CeO_2 support with high concentration of surface defects. Ce-Zr-Y mixed oxide was shown by Nagai et al. [31] to be effective for inhibiting the sintering of Pt clusters during the high-temperature aging in the oxidative atmosphere by forming Pt-O-Ce bond. Farmer et al. [32] also found that Ag nanoparticles (<1000 atoms) had much higher thermal stability on reduced CeO_2 (111) than on MgO (100), as a result of strong bonding of Ag to both

defects and terraces on CeO_2 (111) surface. In a recent study [33], an additional ability of CeO_2 NR with rich surface defects is to improve the thermal stability of single atom catalysts by trapping Pt noble metals in an atomically dispersed state and hindering the Ostwald ripening of single atoms.

Recently, the facet-dependent reactivity of CeO_2 surfaces ({100}, {110}, and {111}) and the presence of various surface defects in combination with the strong interactions between ruthenium species and CeO_2 support have drawn attention to the catalytic combustion of chlorobenzene, low-temperature CO_2 methanation and ammonia synthesis. For example, Huang et al. [34] elucidated that the better activity of Ru/CeO_2 NR than Ru/CeO_2 NO and Ru/CeO_2 NC for the catalytic combustion of chlorobenzene can be related with more abundant Ru-O-Ce bonds, higher Ru^{4+} concentration, easier surface oxygen mobility, and superior surface reducibility of CeO_2 NR support. Wang et al. [35] used *in-situ* infrared spectroscopy to point out that the copious oxygen vacancies in Ru/CeO_2 NC serve as the active sites to activate CO_2, which can explain the improved low-temperature CO_2 methanation performance. Sakpal et al. [36] also reported that Ru/CeO_2 NR is the most active catalyst for CO_2 methanation due to the highest concentration of oxygen vacancies. Lin et al. [37] discovered that Ru species of low crystallinity and a great number of oxygen vacancies exist on the surface of CeO_2 NR, while large-sized metallic Ru (Ru^0) clusters and low concentration of oxygen vacancies exist on CeO_2 NC. Consequently, Ru/CeO_2 NR presented better performance of ammonia synthesis than Ru/CeO_2 NC. Similar results were also found by Ma et al. [38].

Based on the above findings, the morphology of CeO_2 as a support can remarkably influence the catalytic activity of Ru/CeO_2 catalysts. However, the exact role of CeO_2 is still debatable and the Ru-CeO_2 interactions need further understanding in order to reinforce the reactivity of supported ruthenium catalysts. Furthermore, tuning the catalyst-support interfacial

structure by thermal (redox) treatments also plays a critical role and can influence the catalyst, support and catalyst-support interactions at the atomic level [28, 39-41]. The present study is a more comprehensive and deep-going investigation of our recent finding [42]. Ru catalysts supported on CeO_2 NR, NC and NO were prepared and various thermal treatments (oxidation and reduction treatments) were applied to the Ru/CeO_2 catalysts. The variations of low-temperature CO oxidation activity of the catalysts were correlated with the morphology and surface-terminated crystal planes of nanoscale CeO_2 as well as the structure and oxidation state of Ru components in order to gain deep insights into the metal-support interactions between Ru and CeO_2.

2. Experimental section

2.1 Preparation of supports

The CeO_2 NR and CeO_2 NC supports were synthesized by a hydrothermal method. First, 8 mL of 6.0 M NaOH (VWR, 99%) was dropped into 88 mL of 0.1 M $Ce(NO_3)_3 \cdot 6H_2O$ (Acros Organics, 99.5%) solution in a 200 mL Teflon liner and stirred for ~ 15s. The Teflon liner was then put into a stainless-steel autoclave and sealed tightly. The autoclave was heated and kept at 90 °C for 48 h to obtain CeO_2 NR or 150 °C for 48h to obtain CeO_2 NC respectively. Then the as-prepared supports were washed with DI water (500 mL) and absolute ethanol (50 mL) followed by filtration. Finally, CeO_2 NR and NC powders were obtained after drying at 60 °C for 12 h. CeO_2 NO support was prepared by slowly precipitating 0.1 M $Ce(NO_3)_3 \cdot 6H_2O$ solution with 1.0 M $NH_3 \cdot H_2O$ under vigorous stirring. The precipitate was further homogenized at 70 °C for 1 h on a hot plate with magnetic stirring. Then the precursor was washed with DI water (500 mL) and absolute ethanol (50 mL) before it was separated by filtration. Finally, CeO_2 NO powder was obtained by drying at 60 °C for 12 h and calcined in a box furnace at 700 °C for 2 h.

2.2 Preparation of RuO_x/CeO_2 catalysts

Typically, the loading amount of PGM catalysts is 0.5~1.0 wt% in the literature. In this study, by using 5.0 wt% Ru, we aim to maximize the Ru-CeO_2 interaction and demonstrate its effect on the low-temperature CO catalytic oxidation performance of different shaped CeO_2 supported ruthenium catalysts. 5.0 wt% Ru loading on CeO_2 NR, NC and NO supports were prepared by impregnating different CeO_2 supports with 100 mL aqueous solution of a required $Ru(NO)(NO_3)_3$ (Alfa Aesar) content followed by tuning the pH value of the solution with 0.5 M $NH_3 \cdot H_2O$ solution to ~ 9 (incipient wetness impregnation). After that, the solution mixture was aged under stirring at 80 °C for 4 h, followed by vaporizing water at 100 °C and then further drying overnight. Finally, the obtained samples were calcined in the programmable box furnace at 300 °C for 5 h with a heating ramp of 10 ℃/min to obtain $5Ru/CeO_2$-o (after oxidized treatment) catalysts, where 5 refers to the Ru content in weight percentage (5.0 wt% = $[Ru/(Ru + CeO_2)]_{wt} \times 100\%$). Part of the oxidized catalysts were reduced in a 5.0 vol.% H_2/Ar flow (200 mL min^{-1}) at 300 °C for 5 h with a 10 °C/min heating ramp. After cooling down to room temperature with 5.0 vol.% H_2/Ar flowing, $5Ru/CeO_2$-r (after reduced treatment) catalysts were then obtained.

2.3 Characterizations of RuO_x/CeO_2 catalysts

Powder X-ray diffraction (XRD) analysis was carried out on a Philips X'Pert MPD diffractometer using Cu Kα radiation source (λ = 0.154 nm). The diffraction patterns were collected in a 2θ range between 10° and 90° with a step size of 0.005°/s. The lattice constant and average crystallite sizes of the catalysts were analyzed using the JADE software based on the recorded patterns.

Transmission electron microscopy (TEM) and high-resolution transmission electron microscopy (HRTEM) images were obtained on a FEG-TEM instrument (FEI Tecnai F20)

operated at 200 kV. Aberration-corrected high-angle annular dark field scanning transmission electron microscopy (HAADF-STEM) images and complementary energy dispersive X-ray spectrum imaging (EDS) were collected on JEOL JEM2200FS (200 kV) equipped with a third-order CEOS aberration corrector and a Bruker XFlash silicon drift detector. The TEM samples were first ultrasonic dispersion in ethanol and dropped on an ultrathin carbon on 400 mesh copper grid (Ted Pella Inc.) then dried for analysis.

X-ray photoelectron spectroscopy (XPS) was carried out on a Kratos Axis DLD spectrometer using monochromatic Al Kα radiation (hν = 1486.6 eV) under UHV (10^{-10} Torr). The effects of charging were corrected with respect to the carbon peak C 1s (284.8 eV). The fitting and deconvolution of peak spectra were conducted by the XPSPEAK41 software, using Gaussian-Lorentzian line shape and Shirley background subtraction.

Steady-state X-ray Absorption spectroscopy (XAS) was measured at the beamline 12-BM at the Advanced Photon Source of Argonne National Laboratory. The XAS data were collected using a 13-element germanium solid-state detector under room temperature with fluorescence mode. One ion chamber is placed before the sample and used as the incident X-ray flux reference signal. The Ruthenium foil is used for energy calibration and collecting Ruthenium metal spectrum. The powder samples were dispersed on Kapton tape during the measurement.

In-situ diffuse reflectance infrared Fourier transform spectroscopy (DRIFTS) measurements were carried out on a Nicolet 6700 FTIR spectrometer equipped with Harrick Praying Mantis DRIFTS accessory. All the spectra were collected by averaging 64 scans continuously collected with a resolution of 4 cm^{-1}. In CO adsorption experiments, the catalyst surface was fed with 100 mL/min Ar flow at 200 ℃ for 30 min in order to remove moisture prior to each experiment. After cooling down to 30 ℃, the background was collected at the same flow.

The feeding gas was then switched to 100 mL/min 1 vol.% CO-99 vol.% Ar mixture for 20 or 35 min, after which the flow was switched back to 100 mL/min Ar for another 30 min. In CO oxidation testing, the catalyst went through the same pretreatment as for the CO adsorption experiments. After background collection conducted at 30 ℃ with 100 mL/min Ar flow, the feed gas was switch to a 100 mL/min 1 vol.% CO-20 vol.% O_2-79 vol.% Ar with the temperature ramping from 30 to 150 °C with a heating rate of 5 °C/min. The temperature was held at 150 ℃ for another 10 min before the end of the experiment.

The single point BET surface area of the catalysts was measured by nitrogen physisorption at ~77 K. Hydrogen temperature programmed reduction (H_2-TPR) was performed using a AutoChem™ II 2920 chemisorption analyzer (Micromeritics). The powder samples of ~ 100 mg were put into a U-type quartz tube followed by heating from 30 to 900 °C at a 10 °C/min ramping rate. A 10 vol.% H_2-90 vol.% Ar gas mixture (50 mL/min) was flown through the sample tube. Cu_2O was used as the reference standard to calibrate the TPR profile peak area. Based on the calibrated TPR profile peak area, quantitative H_2 consumption by the catalysts was calculated.

The catalytic performance toward CO oxidation was investigated using a fixed bed plug flow chemical reactor. Typically, the catalyst of ~ 50 mg was packed with the quartz wool and then put into the chemical reactor. The reactant gas mixture consisting of 1 vol.% CO-20 vol.% O_2-79 vol.% He (30 mL/min) was introduced into the chemical reactor. The reaction temperature was programmed from room temperature to 400 °C. An online gas chromatograph (SRI multiple gas analyzer GC, 8610C chassis) system controlled by an Autosampler was employed to analyze the presence of CO and the production of CO_2. The CO conversion was evaluated based on the following equation:

$$\%CO\ conversion = \frac{[CO]_{in} - [CO]_{out}}{[CO]_{in}} \times 100\%$$

where $[CO]_{in}$ is the influent CO concentration and $[CO]_{out}$ is the effluent CO concentration at a certain temperature, respectively.

3. Results and discussion

3.1 X-ray diffraction analysis

Fig. 1 shows the XRD patterns of three CeO_2 supports with different morphologies and RuO_x/CeO_2 catalysts after the oxidation and reduction treatments. From Fig. 1a, all the observed diffraction peaks for CeO_2 supports can be indexed to the cubic fluorite-type CeO_2 structure (JCPDS 34-0394). The average crystallite sizes of three different CeO_2 supports calculated using (111) peak at $2\theta = 29°$ are listed in Table 1. It is obvious that the average crystallite size of CeO_2 NR (4.5 nm) is much smaller than that of CeO_2 NC (22.8 nm) and CeO_2 NO (16.6 nm), which agrees well with the largest BET surface area of CeO_2 NR (105.5 m^2/g) among the three different supports.

Fig. 1b and 1c show the XRD patterns of $5Ru/CeO_2$-o and $5Ru/CeO_2$-r catalysts, respectively. From the expanded regions of the XRD patterns between 30° and 50° (Fig 1d and 1e), the reflections of minor phases were observed which can be assigned to RuO_2 and Ru after oxidation and reduction treatment respectively for the $5Ru/CeO_2$NC and $5Ru/CeO_2$NO samples. The peaks intensity of RuO_2 and Ru for $5Ru/CeO_2$NO was higher than that of $5Ru/CeO_2$NC, but all the intensity signals are very low, hence the averaged crystallite size of RuO_x species cannot be calculated. However, for the $5Ru/CeO_2$NR-o or $5Ru/CeO_2$NR-r samples, besides the characteristic peaks of CeO_2, no diffraction peaks of RuO_2 or Ru were detectable. According to the results of other researchers [34, 37, 38] and our previous investigation [43], at least two possible reasons could relate to the absence of RuO_x peaks from the XRD analysis result: (1) Ru diffused into the

CeO_2 lattice; (2) highly dispersed RuO_x species by forming strong Ru-O-Ce bond at RuO_x-CeO_2 interface. The large surface area and high concentration of surface defects of CeO_2 NR compared to CeO_2 NC and NO, shown in our previous results [25], not only can enhance the dispersion of RuO_x species, but also may further trap or anchor unstable RuO_x species to restrain particle growth during the aftertreatment [33]. Dvořák et al. [44] highlighted that the thermally and chemically stable Pt^{2+} ions are closely related to the step edges on CeO_2 nanocrystals. Zhang et al. [45] found that Au nanoparticles could be anchored by oxygen vacancy clusters on CeO_x. In our results, although RuO_x is not visible for the 5Ru/CeO_2NR samples in the XRD analysis (Fig. 1 d and e), it can be clearly detected in all catalysts samples from the EDS (Fig. S1) and XPS analysis discussed below. These results identify the critical role of support surface structure on the size, dispersion, and coordination environment of catalyst clusters or species.

In Table 1, the average crystallite sizes of CeO_2 in 5Ru/CeO_2 samples were calculated using the XRD (111) peak at $2\theta = 29°$. For the 5Ru/CeO_2NR and 5Ru/CeO_2NO samples, the average crystallite sizes of CeO_2 are slightly larger than those of pure CeO_2 NR and NO because of the sintering during the post thermal treatment. For the 5Ru/CeO_2NC sample, the average crystallite size of CeO_2 is almost the same with that of pure CeO_2 NC. The BET surface areas of 5Ru/CeO_2NC and 5Ru/CeO_2NO catalysts are all smaller than those of pure CeO_2 NC and CeO_2 NO, especially for 5Ru/CeO_2NO catalysts. It is noted that after the reduction treatment of the 5Ru/CeO_2NC and 5Ru/CeO_2NO samples, there is an increase of the BET surface area, possibly a result of redispersion of RuO_x species on the CeO_2. Fernández et al. [46] found a decreased crystallites mean size and disaggregation of large nanorod-like RuO_2 structures to small round-shaped Ru crystallites during a reduction treatment for γ-Al_2O_3 supported RuO_2 particles. However, the BET surface areas (108.4 m^2/g for the oxidized sample and 107.4 m^2/g for the reduced sample)

of 5Ru/CeO_2NR are almost the same with that of CeO_2 NR support (105.5 m^2/g), indicating the high dispersion and thermal stability of CeO_2 NR supported Ru species.

3.2 TEM analysis

According to the low magnification TEM observation (Fig. 2a), CeO_2 NR sample after the loading of ruthenium and thermal treatments has a length of 40-100 nm and a diameter of 5-20 nm, which is a little shorter than pure CeO_2 NR. The distribution of Ru species on CeO_2 NR was determined by HAADF-STEM. As shown in Fig. 2b and 2c, the HAADF-STEM images of the CeO_2 NR support confirm a rough {111} termination surface with a large number of defects, including steps and voids. Mock et al. [25] suggested that "defected" surface of CeO_2 NR support can improve the metal-oxide support interaction and thus lead to higher low-temperature catalytic activity for CeO_2 NR-supported transition metal catalysts. From Fig. 2d, the surface of CeO_2 NR presents d_{111} = 3.31 Å. After calculation of the lattice constant *a* of the surface of CeO_2 NR from d_{111} spacing using $a = d_{111}\sqrt{(h^2 + k^2 + l^2)} = d_{111}\sqrt{3}$, the lattice constant is 0.573 nm. It is important to notice that the surface of CeO_2 NR exhibits lattice expansion compared to the lattice constant (0.541 nm) of bulk CeO_2, which is resulted from the reduction of Ce^{4+} to Ce^{3+} (Ce^{3+} radius: 1.143 Å; Ce^{4+} radius: 0.97 Å) when CeO_2 is doped with Ru [47] and corresponding O vacancies at the surface of CeO_2 NR [48]. The lattice expansion is also observed in the XRD result (Fig. S2b). The reversible change of the Ce valence between Ce^{4+} and Ce^{3+} is an important feature of CeO_2-based nanostructures, especially on the surface along with oxygen vacancies formation, which is the key to the good catalytic performance [20, 49, 50].

Due to the thickness of the support and high atomic number of Ce relative to Ru (atomic number for Ru: 44 and Ce: 58), in some cases, the distribution of atomic or small cluster Ru species is difficult to observe based on the Z-contrast of the HAADF-STEM image. However, the STEM-

EDS elemental mappings (Fig. 3) confirm the presence of Ru across the CeO_2NR-r support and the apparent absence of Ru particles in the high-resolution STEM images shows that ruthenium components are present as a highly dispersed RuO_x species over the CeO_2 NR or diffuse into the lattice of CeO_2 NR support. Similar results were also presented by Guo et al [29].

Fig. S3 shows the TEM and HRTEM results of the supported 5Ru/CeO_2NC-r and 5Ru/CeO_2NO-r catalysts. The CeO_2 NC and NO supports maintain their initial morphology after loading the Ru species (Fig. S3a and S3c). For the 5Ru/CeO_2NC-r sample (Fig. S3b), both large-sized particles with an average diameter of 2-3 nm and some small clusters are observed on the surface of CeO_2 NC. Those are attributed to the supported RuO_x species, which will be discussed in the XPS analysis below. For the 5Ru/CeO_2NO-r sample (Fig. S3d), the RuO_x particles appear on the surface of CeO_2 NO. From Fig. 4, the RuO_x species can be found to dispersed unevenly in the 5Ru/CeO_2NO-r sample, suggesting a weak interaction between the RuO_x species and CeO_2 NO support. For the oxidized samples, TEM results of the supported 5Ru/CeO_2NR-o, 5Ru/CeO_2NC-o and 5Ru/CeO_2NO-o catalysts are shown in Fig. S4.

3.3 XPS analysis

Fig. 5a shows the XPS spectra of Ru 3d for the 5Ru/CeO_2NR-o and 5Ru/CeO_2NR-r samples. The oxidation states of Ru were analyzed using Ru $3d_{5/2}$ peaks, which are intense and appropriate for the energy shifts study but overlapping with C 1s peaks. Three different components at around 281.0, 282.1 and 282.7 eV can be assigned to Ru^{4+}, Ru^{n+} and Ru^{6+}, respectively. The components at 284.8 and 288.5 eV are for C 1s peaks. Both of the samples have the component Ru^{4+} at around 281.0 eV, which fits well with the position of crystalline RuO_2 [51] or RuO_2 thin films [52] and thin surface layers formed on the metallic Ru [53]. The difference is that the 5Ru/CeO_2NR-o sample shows the Ru $3d_{5/2}$ peak at 282.7 eV (Ru^{6+}), whereas the

5Ru/CeO_2NR-r sample shows the Ru $3d_{5/2}$ peak at 282.1 eV (Ru^{n+}). Chan et al. [54] attributed the higher binding-energy component at around 282.7 eV to RuO_3 [55]. They studied the oxidation of ruthenium at ambient pressure (1 atm) and elevated temperatures (25-300 °C) by surface-enhanced Raman spectroscopy (SERS) combined with XPS. They confirmed the formation of RuO_3 via the appearance of an 800 cm^{-1} SERS band at 200 °C corresponding to the appearance of a Ru $3d_{5/2}$ peak at 282.6 eV. Furthermore, the relatively rapid cooling process after the RuO_2 film deposition can also promote the formation of RuO_3 species on the surface [56].

For the Ru $3d_{5/2}$ peak at 282.1 eV of the 5Ru/CeO_2NR-r sample, there is a clear peak shift in comparison with the Ru $3d_{5/2}$ peak at 281.0 eV corresponding to Ru^{4+} in RuO_2, indicating different coordination environments (or electronic structure) of Ru ions in these two samples. Singh et al. [47] and Kurnatowska et al. [57] both observed a similar shift of Ru 3d peaks to higher binding energy in $Ce_{0.95}Ru_{0.05}O_2$ and $Ce_{0.89}Ru_{0.11}O_2$, respectively. Based on Kurnatowska et al. [57] and Bolzan et al. [58], Ru^{4+} ions in RuO_2 are coordinated with six oxygen ions by four long Ru-O (0.19857 nm) and two short Ru-O (0.19414 nm). It is quite different from the eight coordination of Ce^{4+} in CeO_2 with eight Ce-O (0.2343 nm), so the observed energy shift of Ru 3d peaks is possibly due to the replacement of Ru for Ce site in CeO_2 lattice. According to [59, 60], different coordination environments of Ru ions in RuO_2 (rutile structure) and in CeO_2 (fluorite structure) cause the energy shift and in both situations they believe the charge of Ru is 4+. Therefore, one possible form of Ru^{n+} here is corresponding to the Ru diffusion into CeO_2 lattice and Ru substitution at the Ce sites, which has +4 oxidation state.

On the other hand, the shift of Ru 3p peaks to higher binding energy was also observed by Wang et al. for the interface engineered Ru–Co_3O_4 catalysts with respect to pure Ru [61], and they attributed this phenomenon to the charge transfer from Ru to Co_3O_4 at the interface. According to

the result of Guo et al. [29], the charge density of RuO_x species can be affected by the interfacial charge transfer between RuO_x species and CeO_2 support and the oxidation states of Ru are related to the strength of electronic interaction of strong metal-support interactions (SMSI). They found that Ru single atoms on CeO_2 support exhibit a stronger electronic interaction compared to Ru nanoclusters and nanoparticles. So another possible explanation of the peak shift for Ru 3d, is that Ru^{n+} is in the form of Ru-O-Ce bond over CeO_2 surface or at the RuO_x-CeO_2 interface via electron transfer (Referred as Ru^{n+}; $4 \leq n \leq 6$). The Raman spectra also demonstrate the existence of the Ru-O-Ce structure on 5Ru/CeO_2NR-r (Fig. S5). Based on the discussion above, in both cases, after the reduction treatment, either the changed coordination environments of Ru in CeO_2 lattice or the Ru-O-Ce bond at the interface could result in the Ru 3d5/2 peak shift to higher binding energy.

As shown in Fig. 5b, both 5Ru/CeO_2NC-r and 5Ru/CeO_2NO-r exhibit three Ru $3d_{5/2}$ peaks at 280.0, 281.0 and 282.1 eV that can be assigned to Ru^0 [34], Ru^{4+} and Ru^{n+}, respectively; 5Ru/CeO_2NR-r shows only two Ru $3d_{5/2}$ peaks at 281.0 and 282.1 eV that can be assigned to Ru^{4+} and Ru^{n+}, respectively. Based on the XPS spectra of Ru 3d for 5Ru/CeO_2 catalysts with different morphologies after oxidation treatment (Fig. S6), the oxidation state of Ru species on CeO_2 NR support is mainly Ru^{6+}. However, the oxidation states of Ru species on CeO_2 NC and NO supports are Ru^{4+} coexisting with Ru^{6+}.

It is obvious that the oxidation state of Ru species on CeO_2 is support morphology (exposed crystal plane) dependent. After reduction treatment, Ru^{n+} species predominates the 5Ru/CeO_2NR-r sample, while metallic Ru nanoclusters or nanoparticles emerge in the 5Ru/CeO_2NC-r and 5Ru/CeO_2NO-r samples. Specifically, the content of Ru^{n+} species follows 5Ru/CeO_2NR-r > 5Ru/CeO_2NC-r $\approx$ 5Ru/CeO_2NO-r (Table 2). The result is also in accord with the XRD and TEM observations that no metallic Ru peaks (XRD pattern) or Ru nanoclusters/nanoparticles (TEM and

STEM images) are found for the 5Ru/CeO_2NR-r sample. The presence of nearly a single Ru $3d_{2/5}$ peak (Ru^{n+}) in the 5Ru/CeO_2NR-r sample also proves the homogeneous distribution of Ru with no large RuO_2 phase over the surface. As discussed above, to be specific, Ru^{n+} species in this work are most likely in the following two possible forms: (1) Ru^{n+} ions diffusion into the CeO_2 lattice [34, 47, 59, 60], (2) small RuO_x clusters in the form of Ru-O-Ce bond at the interface between RuO_x species and CeO_2 through SMSI [38, 62]. The large available surface area and surface defects such as voids and steps of CeO_2 NR provide the precondition for Ru ions diffusion and forming the strong interaction. In the cases of 5Ru/CeO_2NC-r and 5Ru/CeO_2NO-r, however, there are more metallic Ru as a result of the exposed crystal plane and especially much fewer surface defects, where the RuO_x species are less effectively dispersed and form SMSI. The correlation between the amount of Ru^{n+} ions and the performance of CO oxidation will be discussed in more detail later.

Fig. 6a presents the Ce 3d spectra which consists of four pairs of $3d_{5/2}$ and $3d_{3/2}$ peaks. The peaks labeled v, v′, v″, and v‴ belong to the Ce $3d_{5/2}$, whereas the peaks u, u', u'', and u''' belong to the Ce $3d_{3/2}$. Among the eight peaks, v′ and u' (with the binding energies of 883.4 and 907.0 eV) are arising from the Ce^{3+} oxidation state, while v, v″, v‴, u, u'', and u''' (with the binding energies of 881.6, 888.2, 897.3, 900.1, 907.0 and 916.0 eV) can be assigned to the Ce^{4+} oxidation state [36]. Then the concentrations of Ce^{3+} ions are quantitatively determined by calculating the area ratio of the Ce^{3+} oxidation state peaks to all peaks, giving a value of 13.4%, 16.0% and 13.5% for 5Ru/CeO_2NC-r, 5Ru/CeO_2NR-r and 5Ru/CeO_2NO-r, respectively. Ce^{3+} is most likely formed because of oxygen vacancies in the materials [34, 38]. Ce^{3+} ions may also appear due to the under-coordinated Ce ions on the surface of small CeO_2 crystallites, doping with Ru ions and X-ray induced reduction effects in XPS spectrometer [63].

The O 1s spectra of 5Ru/CeO_2-r catalysts are also evaluated (Fig. 6b). The peak at around 529.0 eV can be assigned to lattice oxygen (O_L); that at around 531.0 eV is attributed to oxygen vacancies (O_V) while that at 533~534 eV can be assigned to hydroxyl oxygen or chemisorbed oxygen (O_C) species. Then the ratio of O_V/O_L is calculated to evaluate the concentration of oxygen vacancies. The values are 0.50, 0.59 and 0.34 for 5Ru/CeO_2NC-r, 5Ru/CeO_2NR-r and 5Ru/CeO_2NO-r, respectively. The results indicate that the concentration of oxygen vacancy defects on the surface of 5Ru/CeO_2NR-r is higher than those on the 5Ru/CeO_2NC-r and 5Ru/CeO_2NO-r, which is in accord with the Ce^{3+} concentration result mentioned above. Both of the diffusion of Ru ions into CeO_2 lattice [47] and forming the Ru-O-Ce at the interface are believed to increase the concentration of oxygen vacancies, which are vital for adsorption/dissociation of oxygen in the CO oxidation reaction [64-66] and play a key role in understanding the reaction mechanism [67]. The Raman spectra also evidence the presence of rich oxygen vacancy and the Ru-O-Ce structure on 5Ru/CeO_2NR-r compared to 5Ru/CeO_2NC-r and 5Ru/CeO_2NO-r (Fig. S5).

3.4 X-ray absorption spectroscopy (XAS) analysis

XAS measurements were recorded with the 5Ru/CeO_2NR-o and 5Ru/CeO_2NR-r samples. Brief inspection of the X-ray absorption near edge structure (XANES) region (Fig. 7a) indicates rather subtle changes for the two samples, where the intensity of the oxidized sample is slightly higher at 22.105~ 22.120 keV region and lower at 22.135 ~ 22.150 keV region than the reduced sample. The similar results were previously reported by Mo et al. [68]. As indicated by the derivative XANES spectra (inset of Fig. 7a), the edge energy of these samples are similar but show prominent blue-shift with respect to Ru foil, suggesting that the valence state of Ru in both samples are higher than Ru^0 but close to each other [69], consistent with XPS results above. In addition, the extended X-ray absorption fine structure (EXAFS) spectra of these samples in R-space were

compared in Fig. 7b. It is interesting to note that the EXAFS spectra of both samples are featured by one peak corresponding to Ru-O with negligible Ru-Ru second shell which was previously observed in RuO_2 [69], suggesting significant difference of Ru coordination in our samples from that of RuO_2, supporting the presence of defect RuO_x, consistent with XPS results. Furthermore, while the Ru-O bond distance remains similar between the oxidized and reduced samples, much smaller peak intensity was observed in the oxidized sample than that in the reduced sample. The reduced peak intensity can be either attributed to the decrease of coordination number at the metal center or the increased disorder around the metal center. This is further supported by the results obtained from the quantitative analysis of these EXAFS spectra (Fig. 7b, Fig. S7, and Table S1) by FEFF fitting with ARTEMIS module Demeter software packages [70] in the K range from 2.1 $Å^{-1}$ to 10.2 $Å^{-1}$. For both samples, a much smaller coordination number than 6 ($N < 6$) or abnormally large Debye-Waller factor ($\sigma^2 > 0.01$) has to be used in order to adequately fit these data. Using the same Debye-Waller factor with the maximum value allowed ($\sigma^2 = 0.01$ $Å^2$) for the 5Ru/CeO_2NR-o and 5Ru/CeO_2NR-r samples, which suggests that the fit is ill conditioned, N is higher in the reduced sample (3.67±0.03) than the oxidized sample (2.51±0.02), suggesting a more severe defect in the oxidized sample. Combined these results with XPS spectra of Ru 3d, the Ru element might be in the form of highly dispersed RuO_2 clusters with surface defects RuO_3 across the CeO_2 NR surface in the oxidized sample. Furthermore, the reduction treatment of the sample may have reduced the surface Ru^{6+} to Ru^{n+} ($4 \leq n \leq 6$) by forming Ru-O-Ce bond at the interface between RuO_x species and CeO_2 NR or enforced Ru ions to diffuse into the CeO_2 surface lattice, which is supported by the increased coordination number and slightly increased Ru-O bond distance in the reduced sample (1.99 Å) compared to that in the oxidized sample (1.97 Å).

3.5 Reducibility of 5Ru/CeO_2 Catalysts

Considering the key role of the surface oxygen of CeO_2 in CO oxidation, H_2-TPR was employed to investigate the oxygen release capacity of three CeO_2 supports and $5Ru/CeO_2$ catalysts with different support morphology after the oxidation and reduction treatments, and the result is given in Fig. 8.

Fig. 8a shows the H_2-TPR profiles of CeO_2 NR, NC and NO. Two main reduction peaks centered at 474 ~ 497 °C and 795 ~ 823 °C, correspond to the reduction of surface oxygen (O_s) and bulk oxygen (O_b) of CeO_2, respectively [71]. The H_2 consumption of the O_s and O_b reduction is listed in Table 3. CeO_2 NR exhibits the lowest surface reduction (474 °C) and bulk reduction temperature (795 °C) and largest surface-to-bulk oxygen (O_s/O_b) ratio (1.07) compared to those for CeO_2 NC (0.15) and CeO_2 NO (0.43). The above results show that CeO_2 NR exposed defected (111) plane in our study have the highest amount of active surface oxygen species and are catalytically active support for CO oxidation reaction [72].

The H_2-TPR profiles of the $5Ru/CeO_2$-o samples are shown in Fig. 8b. Generally, there are three regions in the H_2-TPR profiles of CeO_2-supported noble metal catalysts [43]: the region below 200 °C; the region at 200-500 °C corresponding to the reduction of surface oxygen; and the region above 500 °C because of the reduction of bulk oxygen of CeO_2. Table 4 exhibits the hydrogen consumptions in each region. Due to the large H_2 consumption below 200 °C, the latter two regions of the oxidized samples are not clear in Fig. 8b. In the region below 200 °C, the $5Ru/CeO_2$NR-o sample presented two reduction peaks at 92 and 118 °C. For the $5Ru/CeO_2$NC-o sample, three reduction peaks appeared at 165, 90 and 124 °C. Only one reduction peak at 134 °C was observed for $5Ru/CeO_2$NO-o sample. The presence of the multiple peaks below 200 °C indicates at least two different existing states of RuO_2: the well-dispersed RuO_x species which can be reduced at a lower temperature and the well-crystallized RuO_2 which can be reduced at a

relatively higher temperature [35, 43]. Compared with the 5Ru/CeO_2NC-o and 5Ru/CeO_2NO-o samples, 5Ru/CeO_2NR-o shows a much stronger lower-temperature reduction peak with a significant enhancement in the H_2 consumption (Table 4). Huang et al. [34] ascribed this phenomenon to the relaxing Ce-O bond strongly bounded with Ru species, which is similar to the case in Au/CeO_2NR [23].

The H_2-TPR profiles of the 5Ru/CeO_2-r samples are shown in Fig. 8c. The three regions described above are also observed here. Below 200 °C, only one peak shown at 84, 60 and 62 °C for the 5Ru/CeO_2NR-r, 5Ru/CeO_2NC-r and 5Ru/CeO_2NO-r samples, respectively. This peak was ascribed to the strong RuO_x-CeO_2 interaction. The electron-rich interfacial oxygen ions on the CeO_2 support after receiving the donated electrons from Ru species can be easily released and utilized for CO oxidation [67]. Although the strong RuO_x-CeO_2 interaction peaks of the 5Ru/CeO_2NC-r and 5Ru/CeO_2NO-r samples appear at a lower temperature than that at which the peak of the 5Ru/CeO_2NR-r appears, it is clear that the H_2 consumption of 5Ru/CeO_2NR-r starts at much lower temperature than 5Ru/CeO_2NC-r and 5Ru/CeO_2NO-r (from enlarged figure shown below), which means the surface oxygen of 5Ru/CeO_2NR-r can be more easily reduced because of the existence of stronger RuO_x-CeO_2 interaction (Ru-O-Ce structure and Ru^{n+} ions diffused into the lattice) across the surface of 5Ru/CeO_2NR-r. The total H_2 consumption of the 5Ru/CeO_2NR-r sample was nearly tenfold higher than the other two counterparts below 200 °C (Table 3), indicating that much more active surface oxygen can be provided and used at low temperature for CO oxidation. In addition, the peaks of hydrogen consumption of 5Ru/CeO_2NC-r (60 °C), 5Ru/CeO_2NO-r (62 °C) appeared at lower temperature, presumably due to the presence of surface metallic Ru, similar result was also observed in Pd/CeO_2 by Hu et al. [73].

The oxygen contents of the 5Ru/CeO_2 NR-o and 5Ru/CeO_2 NR-r samples are also evaluated based on the following equation and showed in Table 4.

$$CeO_2 + (2-x)H_2 \rightarrow CeO_x + (2-x)H_2O$$

From Table 4, the oxygen content x in CeO_x of the 5Ru/CeO_2 NR-o and 5Ru/CeO_2 NR-r samples are 1.43 ($CeO_{1.43}$) and 1.61 ($CeO_{1.61}$), respectively, which suggests final CeO_x materials with x close to 1.5 (Ce_2O_3). Based on the phase diagram, this low oxygen content x is unreasonable (in general x>1.75). It can be explained by that the reduction from CeO_2 to CeO_x isn't the only source responsible for hydrogen uptake. Other possible reasons include the reduction of RuO_x, the presence of residual carbonates/nitrates species [74], homolytic (OHs) and heterolytic products (Ce−H and OH) [75]. All of these species can consume hydrogen during H_2-TPR experiment, which could result in the low oxygen content x values in CeO_x.

3.6 CO oxidation activity measurements

Fig. 9 shows the CO oxidation activity of the 5Ru/CeO_2 samples with different support morphologies after the oxidation and reduction treatments. CO oxidation conversion light-off curves of the different shaped 5Ru/CeO_2 samples after oxidation treatment are shown in Fig. 9a. All of the samples achieve 100% CO conversion at ~ 200 °C. Only a slightly better oxidation performance, in terms of the temperature of 10%-conversion (T_{10}), was obtained for the 5Ru/CeO_2NR-o sample: 5Ru/CeO_2NR-o (71 °C) < 5Ru/CeO_2NC-o (96 °C) ≈ 5Ru/CeO_2NO-o (99 °C). The support morphology does not have an obvious effect on the catalytic activity of 5Ru/CeO_2-o samples. After reduction treatment, the 5Ru/CeO_2 samples showed significantly enhanced low-temperature CO conversion than that after oxidation treatment, indicating a strong catalyst activation by reduction treatment and obvious support morphology effect (Fig. 9b). Specifically, the catalytical performance with regard to the temperature of half-conversion (T_{50}) is

in the order (Table 1): 5Ru/CeO_2NR-r (50 °C) << 5Ru/CeO_2NC-r (112 °C) ≈ 5Ru/CeO_2NO-r (104 °C). All the T_{50} for the reduced samples are lower than the samples after oxidation treatment, especially for the CeO_2NR supported sample. It is also worth noticing that the 5Ru/CeO_2NR-r sample offers nearly total CO conversion at temperatures as low as 100 °C, about 50 °C lower than the 5Ru/CeO_2NC-r and 5Ru/CeO_2NO-r samples. In particular, the 5Ru/CeO_2NR-r sample exhibits ~ 9% CO conversion at room temperature, the best low-temperature activity among the 5Ru/CeO_2-r catalysts with three different morphologies, while the 5Ru/CeO_2NC-r and 5Ru/CeO_2NO-r samples achieve 10% CO conversion at 74 °C. The better CO conversion performance for the CeO_2 NR sample has already been reported previously [73, 76-78]. For the purpose of comparison, a series of reference samples of 5Ru/CeO_2NR-r-(2^{nd} method), 5Ru/Al_2O_3-r, 5Ru/SiO_2-r and 5Ru/ZnO-r were also evaluated for the same reaction, as shown in Fig. S8. The 5Ru/CeO_2NR-r-(2^{nd} method, mechanical mixing) sample shows much lower activity than the 5Ru/CeO_2NR-r sample prepared by incipient wetness impregnation. It is obvious that the preparation method can influence the Ru-CeO_2NR interaction and further the CO oxidation catalytic activity of 5Ru/CeO_2NR catalyst. The activities of 5Ru/Al_2O_3-r, 5Ru/SiO_2-r and 5Ru/ZnO-r samples are much worse than the 5Ru/CeO_2-r samples, suggesting the vital role of supports in promoting the catalyst activity and the synergetic effect of Ru-CeO_2 in CO oxidation activity for 5Ru/CeO_2NR, 5Ru/CeO_2NC and 5Ru/CeO_2NO samples. Low-temperature CO conversion rates (normalized by the catalyst weight) were also calculated to further compare the activity of 5Ru/CeO_2-r samples. At ~ 55 °C, the 5Ru/CeO_2NR-r sample displays a rate of 2.7×10^{-4} mol CO $g_{cat}^{-1}s^{-1}$, while the 5Ru/CeO_2NC-r and 5Ru/CeO_2NO-r samples presented lower values of 2.9×10^{-5} and 3.0×10^{-5} mol CO $g_{cat}^{-1}s^{-1}$, respectively.

As discussed before, the dominate Ru^{n+} and absence of metallic Ru^0 clusters on the 5Ru/CeO_2NR-r sample indicate a very high Ru dispersion and a unique structure of cationic Ru species, which account for this superior low-temperature catalytic activity. On the contrary, the Ru nanoparticles and less amount of cationic Ru species on the surface of the 5Ru/CeO_2NC-r and 5Ru/CeO_2NO-r samples can reasonably explain the much lower activity of these samples.

Fig. 10 shows the reaction rate r below 20% CO conversion. The apparent activation energies (E_a) for these different shaped 5Ru/CeO_2-o and 5Ru/CeO_2-r are calculated according to the Arrhenius equation and listed in Table 1. The E_a values of 5Ru/CeO_2NO-o, 5Ru/CeO_2NC-o, and 5Ru/CeO_2NR-o were 26.1, 22.2 and 22.3 kJ mol^{-1}, respectively. The E_a values of 5Ru/CeO_2NO-r, 5Ru/CeO_2NC-r, and 5Ru/CeO_2NR-r decreased to 24.8, 20.8 and 19.6 kJ mol^{-1}, respectively. This result suggests that the reduction treatment activated the catalysts.

3.7 *In-situ* DRIFTS Analysis

In-situ diffuse reflectance infrared Fourier transform spectroscopy (DRIFTS) was utilized in detecting the active species and adsorption sites during CO adsorption and CO oxidation reaction.

Fig. 11 shows the time-dependent *in-situ* DRIFTS spectra of CO adsorption on three 5Ru/CeO_2-r samples (NR, NC, NO) at 30 °C. The bands at 2300-2400 cm^{-1} are related with the weakly adsorbed or gaseous CO_2, and the bands at 1800-2300 cm^{-1} are related with the adsorbed and gaseous CO. In the first 35 min for the 5Ru/CeO_2NR-r and 5Ru/CeO_2NO-r samples and the first 20 min for the 5Ru/CeO_2NC-r sample, 1 vol.% CO/Ar stream was flowed first to reach CO saturation coverage (CO adsorption) and the bands at ~2171 and ~2123 cm^{-1} are assigned to gaseous CO, after which the flow was switched back to pure Ar stream.

For 5Ru/CeO_2NR-r, the CO adsorption spectra are characterized by three bands, at ~2120, ~2064 and ~1990 cm^{-1}. Both high-frequency bands (2120/2064 cm^{-1}) are attributed to a multicarbonyl species formed by the binding of two or three CO ligands to a $Ru^{\delta+}$ site [79-82]. Assmann et al. [79] and Kantcheva et al. [81] both observed similar bands at 2125/2067 cm^{-1} on Ru/MgO and 2130/2064 cm^{-1} on Ru/SiO_2, respectively, and assigned them to CO adsorbed on oxidized Ru sites. For the band at ~1990 cm^{-1}, its assignment is uncertain in the literature. Assmann et al. [79, 80] assigned it to C-O vibrations of CO adsorbed on oxygen vacancies in the RuO_2 film. Derk et al. [83] and Sharma et al. [59] also found that the CO IR-adsorption band at ~1990 cm^{-1} was unique to Ru-doped CeO_2 ($Ce_{0.95}Ru_{0.05}O_2$, where Ru is in ionic state), while no CO adsorption was observed in CeO_2 supported metallic Ru. In addition, in the DRIFTS study by Derk et al. [83], they also observed three distinct Ru sites for the CO adsorbed on $Ce_{0.95}Ru_{0.05}O_2$ (where Ru is ionic state), and the frequencies of the assigned bands in their work are similar to those identified in Fig. 11. In summary, according to the IR assignments, the majority of Ru is the ionic state in the 5Ru/CeO_2NR-r sample, indicating Ru either diffuses into the CeO_2 lattice or forms Ru-O-Ce bonding at the RuO_x-CeO_2 interface. This is consistent with the XPS observation above. For 5Ru/CeO_2NC-r, apart from the high-frequency bands at ~2120 and ~2073 cm^{-1} with much lower intensity (corresponding to the $Ru^{\delta+}(CO)_x$), there are another two bands at ~2056 and ~1978 cm^{-1}. The band at ~2056 cm^{-1} is ascribed to C-O vibrations of linearly adsorbed CO on Ru^0 sites [83]. This assignment is based on the previous FTIR studies of CO adsorption on Ru(001) single crystals [84] and Ru/Al_2O_3 [85]. The broad shoulder at ~1980 cm^{-1} was assigned to bridged CO bonded to Ru at the Ru-CeO_2 interface [86]. Similar four bands on 5Ru/CeO_2NC-r are also observed on 5Ru/CeO_2NO-r, except an additional weak band at ~2025 cm^{-1}, which is assigned to linearly

adsorbed CO on Ru^0 sites [85]. The assignments of the bands in these three samples are summarized in Table 5.

In summary, the above DRIFTS spectra results show that the adsorption of CO on three 5Ru/CeO_2-r catalysts is obviously affected by the morphology of the support. On 5Ru/CeO_2NR-r, the CO adsorption sites are mainly on the oxidized Ru sites, while on 5Ru/CeO_2NC-r and 5Ru/CeO_2NO-r, the CO adsorption sites are on the oxidized Ru sites combined with the metallic Ru^0 sites. This is consistent with the XPS result. The CO uptake of Ru sites on different CeO_2 supports was found to be especially distinct in the following order: CO-(5Ru/CeO_2NR-r) > CO-(5Ru/CeO_2NC-r) $\approx$ CO-(5Ru/CeO_2NO-r), suggesting more CO adsorption sites on 5Ru/CeO_2NR-r than the other two samples. Also noted in the DRIFTS spectra of CO adsorbed on three 5Ru/CeO_2-r samples at 30 °C (Fig. 11a), CO_2 is formed for the 5Ru/CeO_2NR-r sample during exposure to CO, indicating that adsorbed CO readily reacts with the rich active oxygen species over CeO_2 NR support to form CO_2. However, for the 5Ru/CeO_2NC-r and 5Ru/CeO_2NO-r samples, there is no sign of CO_2 formation during exposure of CO to the samples for 1 h. We can conclude that CO adsorbed on the oxidized Ru sites for the 5Ru/CeO_2NR-r sample was more reactive than that adsorbed on the Ru sites for the 5Ru/CeO_2NC-r and 5Ru/CeO_2NO-r samples. By correlating this finding from *in situ* DRIFTS with the low-temperature CO oxidation reactivity of these catalysts (Fig. 9b) and the amount of Ru^{n+} species analyzed from the XPS result (Fig. 5b and Table 2), we infer that the oxidized Ru sites (Ru^{n+} sites) on three 5Ru/CeO_2-r samples, are active sites which are responsible for low-temperature CO oxidation. Similarly, Nie et al. [87] reported that platinum ions (Pt^{2+}) atomically dispersed on CeO_2 act as active site responsible for the improved low-temperature CO oxidation reactivity.

Fig. 12 shows the *in-situ* DRIFTS spectra of CO oxidation on three 5Ru/CeO_2-r samples from 30 °C to 150 °C. By comparison of the DRIFTS spectra of CO oxidation on three 5Ru/CeO_2-r samples from 30 °C to 150 °C, the 5Ru/CeO_2NR-r sample has significantly larger CO uptake than the other two samples at 30 °C and the intensity of the corresponding peaks appear to continuously decrease from 30 °C to 150 °C. The CO uptake of three 5Ru/CeO_2-r samples is closely related to the formation of CO_2. The bands developing at 2300-2400 cm^{-1} are due to the formation of gaseous CO_2. The onset temperature of gaseous CO_2 formation over three 5Ru/CeO_2-r catalysts are significantly different. For the 5Ru/CeO_2NR-r sample, CO_2 signals appear at around 30~50 °C in company with the largest CO uptake. As for the 5Ru/CeO_2NC-r and 5Ru/CeO_2NO-r samples, there is no signal of CO_2 formation until 105-110 °C. This much lower formation temperature of CO_2 for 5Ru/CeO_2NR-r is in qualitative agreement with the superior activity of CO oxidation shown in Fig. 9b. In addition, due to possible inhibition effect, the DRIFTS results of CO adsorption and CO oxidation are quite different.

From the obtained results, Fig. 13 illustrates conceivable interaction models between Ru species and CeO_2 supports with three different morphologies after reduction treatment. Compared with the 5Ru/CeO_2NC-r and 5Ru/CeO_2NO-r samples, the superiority of 5Ru/CeO_2NR-r can receive a consistent explanation. From the TEM results, our CeO_2 NR expose rough {111} surface with a large number of defects, comprising steps and voids [25, 76]. These “defected” surfaces of CeO_2 NR are advantageous to anchor/stabilize Ru species in small crystal size and high dispersion. As for CeO_2 NC and NO, no large amount of anchoring/trap sites are provided. Thus the larger surface area and defect-rich surfaces of CeO_2 NR help loaded Ru species interact strongly with CeO_2 NR and disperse homogeneously by Ru-O-Ce bonds formation and concomitant partial Ru^{n+} ions diffusion into the surface CeO_2 NR lattices. However, the weak Ru-CeO_2 interaction between

Ru species and CeO_2 NC or NO induces the formation of large metallic Ru^0 particles and small RuO_2 clusters on the surface of 5Ru/CeO_2NC-r and 5Ru/CeO_2NO-r samples. The DFT calculations [86] as well as experiments [57] showed that the Ru substitution in CeO_2 lattice can elongate Ce-O and Ru-O bond and decrease the oxygen vacancy formation energy, which are beneficial to improved low-temperature CO oxidation activity. In addition, the well-dispersed Ru species in the form of Ru-O-Ce bonds are highly delicate and its oxygen is mobile and active for CO oxidation [88]. A similar explanation was also provided in the case of Pd/CeO_2 catalyst [30]. Two cationic palladium species determined the high low-temperature CO conversion performance of the Pd/CeO_2 catalyst: the surface interaction phase ($Pd_xCe_{1-x}O_{2-\delta}$) and surface structures PdO_x/Pd-O-Ce, which are formed as a result of the strong interaction between the palladium species and high concentration of defects and a certain structure of the CeO_2 NR support. In our case, the enriched surface defects on the exposed {111} planes of CeO_2 NR support contribute to the cationic ruthenium species formation, which is considered as the decisive factor for the superior low-temperature activity of CeO_2 NR supported RuO_x catalysts.

The above discussions concerning structure-reactivity relationship are well demonstrated by the perfect relations between either the H_2 consumption < 100 °C or low-temperature CO oxidation activity (T_{10}) and the amount of Ru^{n+} species (Ru-O-Ce structure and Ru^{n+} ions diffused into the surface lattice) on different shaped 5Ru/CeO_2-r catalysts (Fig. 14).

4. Conclusion

In conclusion, three nanostructure 5Ru/CeO_2 catalysts with different support morphologies were prepared and applied in CO oxidation. It was observed that the support morphology and Ru valence state greatly affected the CO oxidation activity. The CeO_2 NR supported Ru catalyst

showed the strongest Ru-CeO_2 interaction, enhanced reducibility and the highest low-temperature CO oxidation activity with ~9% CO conversion at around room temperature. However, with regards to 5Ru/CeO_2NC-r and 5Ru/CeO_2NO-r, the weak Ru-CeO_2 interactions with CeO_2 NC and NO supports limited the reducibility and CO oxidation catalytic activity at low temperatures. The variances in the interactions and properties of the 5Ru/CeO_2 catalysts can be attributed to the surface structure of CeO_2 supports. TEM results indicated that CeO_2 NR predominantly exposed surface defects enriched {111} planes, while NO and NC were enclosed by relatively smooth {111} planes and {100} planes, respectively. For this reason, CeO_2 NR exhibited distinct advantage over NO and NC to form strong metal-support interactions and anchor and stabilize RuO_x species. XPS revealed that partial ruthenium species were isolated on the surface in metal particles state on 5Ru/CeO_2NC-r and 5Ru/CeO_2NO-r. However, Ru^{n+} ions predominated in the 5Ru/CeO_2NR-r catalyst, which could diffuse into the surface lattices and form Ru-O-Ce structure on the CeO_2 NR surface then aid the oxygen vacancies enhancement. As evidenced by *in-situ* DRIFTS, these cationic Ru species are vitally important for the superior low-temperature activity of CeO_2NR-supported RuO_x catalysts.

Acknowledgment

This work is supported by National Science Foundation (CHE-1657943 and CBET-1856729) and American Chemical Society Petroleum Research Fund (#52323). This project also receives partial financial support from Alabama Water Institute and Alabama Transportation Institute. The use of TEM facilities at the Central Analytical Facility at The University of Alabama is gratefully acknowledged. Aberration-corrected STEM-EDS was conducted at the Center for Nanophase Materials Sciences, which is a DOE Office of Science User Facility.

Supporting Information

Experimental materials and methods, the results of EDS, XRD Rietveld analysis, TEM/HRTEM, Raman spectra, XPS spectra, XAS spectra, and CO conversion performance.

References

[1] Trovarelli, A.; Fornasiero, P., Catalysis by ceria and related materials Catalytic Science Series, vol. 12, Imperial College Press, UK, 2013.

[2] Adijanto, L.; Sampath, A.; Yu, A. S.; Cargnello, M.; Fornasiero, P.; Gorte, R. J.; Vohs, J. M., Synthesis and Stability of Pd@CeO_2 Core–Shell Catalyst Films in Solid Oxide Fuel Cell Anodes. *ACS Catal.* **2013,** *3*, 1801-1809.

[3] Chen, Y.; deGlee, B.; Tang, Y.; Wang, Z.; Zhao, B.; Wei, Y.; Zhang, L.; Yoo, S.; Pei, K.; Kim, J. H.; Ding, Y.; Hu, P.; Tao, F. F.; Liu, M., A robust fuel cell operated on nearly dry methane at 500 °C enabled by synergistic thermal catalysis and electrocatalysis. *Nat. Energy* **2018,** *3*, 1042-1050.

[4] Jasinski, P.; Suzuki, T.; Anderson, H. U., Nanocrystalline undoped ceria oxygen sensor. *Sens. Actuator B-Chem.* **2003,** *95*, 73-77.

[5] Asati, A.; Santra, S.; Kaittanis, C.; Nath, S.; Perez, J. M., Oxidase-Like Activity of Polymer-Coated Cerium Oxide Nanoparticles. *Angew. Chem.* **2009,** *121*, 2344-2348.

[6] Tarnuzzer, R. W.; Colon, J.; Patil, S.; Seal, S., Vacancy Engineered Ceria Nanostructures for Protection from Radiation-Induced Cellular Damage. *Nano Lett.* **2005,** *5*, 2573-2577.

[7] Carrettin, S.; Concepción, P.; Corma, A.; López Nieto, J. M.; Puntes, V. F., Nanocrystalline CeO_2 Increases the Activity of Au for CO Oxidation by Two Orders of Magnitude. *Angew. Chem. Int. Ed.* **2004,** *43*, 2538-2540.

[8] Setiabudi, A.; Chen, J.; Mul, G.; Makkee, M.; Moulijn, J. A., CeO_2 catalysed soot oxidation: The role of active oxygen to accelerate the oxidation conversion. *Appl. Catal., B* **2004,** *51*, 9-19;

[9] Delimaris, D.; Ioannides, T., VOC oxidation over MnO_x–CeO_2 catalysts prepared by a combustion method. *Appl. Catal., B* **2008,** *84*, 303-312.

[10] Fu, Q.; Saltsburg, H.; Flytzani-Stephanopoulos, M., Active Nonmetallic Au and Pt Species on Ceria-Based Water-Gas Shift Catalysts. *Science* **2003,** *301*, 935.

[11] Concepción, P.; Corma, A.; Silvestre-Albero, J.; Franco, V.; Chane-Ching, J. Y., Chemoselective Hydrogenation Catalysts: Pt on Mesostructured CeO_2 Nanoparticles Embedded within Ultrathin Layers of SiO_2 Binder. *J. Am. Chem. Soc.* **2004,** *126*, 5523-5532.

[12] Otsuka, K.; Wang, Y.; Sunada, E.; Yamanaka, I., Direct Partial Oxidation of Methane to Synthesis Gas by Cerium Oxide. *J. Catal.* **1998,** *175*, 152-160.

[13] Montini, T.; Melchionna, M.; Monai, M.; Fornasiero, P., Fundamentals and Catalytic Applications of CeO_2-Based Materials. *Chem. Rev.* **2016,** *116*, 5987-6041.

[14] Wang, R.; Crozier, P. A.; Sharma, R., Structural Transformation in Ceria Nanoparticles during Redox Processes. *J. Phys. Chem. C* **2009,** *113*, 5700-5704.

[15] Mai, H.-X.; Sun, L.-D.; Zhang, Y.-W.; Si, R.; Feng, W.; Zhang, H.-P.; Liu, H.-C.; Yan, C.-H., Shape-Selective Synthesis and Oxygen Storage Behavior of Ceria Nanopolyhedra, Nanorods, and Nanocubes. *J. Phys. Chem. B* **2005,** *109*, 24380-24385.

[16] Wang, R.; Dangerfield, R., Seed-mediated synthesis of shape-controlled CeO_2 nanocrystals. *RSC Adv.* **2014,** *4*, 3615-3620.

[17] Yuan, Q.; Duan, H.-H.; Li, L.-L.; Sun, L.-D.; Zhang, Y.-W.; Yan, C.-H., Controlled synthesis and assembly of ceria-based nanomaterials. *J. Colloid Interface Sci.* **2009,** *335*, 151-167.

[18] Aneggi, E.; Wiater, D.; de Leitenburg, C.; Llorca, J.; Trovarelli, A., Shape-Dependent Activity of Ceria in Soot Combustion. *ACS Catal.* **2014,** *4*, 172-181.

[19] Ha, H.; Yoon, S.; An, K.; Kim, H. Y., Catalytic CO Oxidation over Au Nanoparticles Supported on CeO_2 Nanocrystals: Effect of the Au–CeO_2 Interface. *ACS Catal.* **2018**, *8*, 11491-11501.

[20] Trovarelli, A.; Llorca, J., Ceria Catalysts at Nanoscale: How Do Crystal Shapes Shape Catalysis? *ACS Catal.* **2017,** *7*, 4716-4735.

[21] Nolan, M.; Grigoleit, S.; Sayle, D. C.; Parker, S. C.; Watson, G. W., Density functional theory studies of the structure and electronic structure of pure and defective low index surfaces of ceria. *Surf. Sci.* **2005,** *576*, 217-229.

[22] Nolan, M.; Parker, S. C.; Watson, G. W., The electronic structure of oxygen vacancy defects at the low index surfaces of ceria. *Surf. Sci.* **2005,** *595*, 223-232.

[23] Si, R.; Flytzani-Stephanopoulos, M., Shape and Crystal-Plane Effects of Nanoscale Ceria on the Activity of Au-CeO_2 Catalysts for the Water–Gas Shift Reaction. *Angew. Chem. Int. Ed.* **2008,** *47*, 2884-2887.

[24] Agarwal, S.; Lefferts, L.; Mojet, B. L.; Ligthart, D. A. J. M.; Hensen, E. J. M.; Mitchell, D. R. G.; Erasmus, W. J.; Anderson, B. G.; Olivier, E. J.; Neethling, J. H.; Datye, A. K., Exposed Surfaces on Shape-Controlled Ceria Nanoparticles Revealed through AC-TEM and Water–Gas Shift Reactivity. *ChemSusChem* **2013,** *6*, 1898-1906.

[25] Mock, S. A.; Sharp, S. E.; Stoner, T. R.; Radetic, M. J.; Zell, E. T.; Wang, R., CeO_2 nanorods-supported transition metal catalysts for CO oxidation. *J. Colloid Interface Sci.* **2016,** *466*, 261-267.

[26] Ta, N.; Liu, J.; Chenna, S.; Crozier, P. A.; Li, Y.; Chen, A.; Shen, W., Stabilized Gold Nanoparticles on Ceria Nanorods by Strong Interfacial Anchoring. *J. Am. Chem. Soc.* **2012,** *134*, 20585-20588.

[27] Satsuma, A.; Yanagihara, M.; Ohyama, J.; Shimizu, K., Oxidation of CO over Ru/Ceria prepared by self-dispersion of Ru metal powder into nano-sized particle. *Catal. Today* **2013,** *201*, 62-67.

[28] Aitbekova, A.; Wu, L.; Wrasman, C. J.; Boubnov, A.; Hoffman, A. S.; Goodman, E. D.; Bare, S. R.; Cargnello, M., Low-Temperature Restructuring of CeO_2-Supported Ru Nanoparticles Determines Selectivity in CO_2 Catalytic Reduction. *J. Am. Chem. Soc.* **2018,** *140*, 13736-13745.

[29] Guo, Y.; Mei, S.; Yuan, K.; Wang, D.-J.; Liu, H.-C.; Yan, C.-H.; Zhang, Y.-W., Low-Temperature CO_2 Methanation over CeO_2-Supported Ru Single Atoms, Nanoclusters, and Nanoparticles Competitively Tuned by Strong Metal–Support Interactions and H-Spillover Effect. *ACS Catal.* **2018,** *8*, 6203-6215.

[30] Slavinskaya, E. M.; Gulyaev, R. V.; Zadesenets, A. V.; Stonkus, O. A.; Zaikovskii, V. I.; Shubin, Y. V.; Korenev, S. V.; Boronin, A. I., Low-temperature CO oxidation by Pd/CeO_2 catalysts synthesized using the coprecipitation method. *Appl. Catal., B* **2015,** *166-167*, 91-103.

[31] Nagai, Y.; Hirabayashi, T.; Dohmae, K.; Takagi, N.; Minami, T.; Shinjoh, H.; Matsumoto, S. i., Sintering inhibition mechanism of platinum supported on ceria-based oxide and Pt-oxide–support interaction. *J. Catal.* **2006,** *242*, 103-109.

[32] Farmer, J. A.; Campbell, C. T., Ceria Maintains Smaller Metal Catalyst Particles by Strong Metal-Support Bonding. *Science* **2010,** *329*, 933.

[33] Jones, J.; Xiong, H.; DeLaRiva, A. T.; Peterson, E. J.; Pham, H.; Challa, S. R.; Qi, G.; Oh, S.; Wiebenga, M. H.; Pereira Hernández, X. I.; Wang, Y.; Datye, A. K., Thermally stable single-atom platinum-on-ceria catalysts via atom trapping. *Science* **2016,** *353*, 150-154.

[34] Huang, H.; Dai, Q.; Wang, X., Morphology effect of Ru/CeO_2 catalysts for the catalytic combustion of chlorobenzene. *Appl. Catal., B* **2014,** *158-159*, 96-105.

[35] Wang, F.; Li, C.; Zhang, X.; Wei, M.; Evans, D. G.; Duan, X., Catalytic behavior of supported Ru nanoparticles on the {100}, {110}, and {111} facet of CeO_2. *J. Catal.* **2015,** *329*, 177-186.

[36] Sakpal, T.; Lefferts, L., Structure-dependent activity of CeO_2 supported Ru catalysts for CO_2 methanation. *J. Catal.* **2018,** *367*, 171-180.

[37] Lin, B.; Liu, Y.; Heng, L.; Wang, X.; Ni, J.; Lin, J.; Jiang, L., Morphology Effect of Ceria on the Catalytic Performances of Ru/CeO_2 Catalysts for Ammonia Synthesis. *Ind. Eng. Chem. Res* **2018,** *57*, 9127-9135.

[38] Ma, Z.; Zhao, S.; Pei, X.; Xiong, X.; Hu, B., New insights into the support morphology-dependent ammonia synthesis activity of Ru/CeO_2 catalysts. *Catal. Sci. Technol* **2017,** *7*, 191-199.

[39] Wang, R.; Fang, M., Improved low-temperature reducibility in ceria zirconia nanoparticles by redox treatment. *J. Mater. Chem.* **2012,** *22*, 1770-1773.

[40] Wang, R.; Crozier, P. A.; Sharma, R., Nanoscale compositional and structural evolution in ceria zirconia during cyclic redox treatments. *J. Mater. Chem.* **2010,** *20*, 7497-7505.

[41] Gänzler, A. M.; Casapu, M.; Maurer, F.; Störmer, H.; Gerthsen, D.; Ferré, G.; Vernoux, P.; Bornmann, B.; Frahm, R.; Murzin, V.; Nachtegaal, M.; Votsmeier, M.; Grunwaldt, J.-D., Tuning the Pt/CeO_2 Interface by in Situ Variation of the Pt Particle Size. *ACS Catal.* **2018,** *8*, 4800-4811.

[42] Li, J.; Liu, Z.; Cullen, D. A.; Wang, R., Ruthenium Diffusion on Different CeO_2 Surfaces: Support Shape Effect. *Microsc. Microanal.* **2019,** *25*, 2198-2199.

[43] Li, J.; Liu, Z.; Wang, R., Support structure and reduction treatment effects on CO oxidation of SiO_2 nanospheres and CeO_2 nanorods supported ruthenium catalysts. *J. Colloid Interface Sci.* **2018,** *531*, 204-215.

[44] Dvořák, F.; Farnesi Camellone, M.; Tovt, A.; Tran, N.-D.; Negreiros, F. R.; Vorokhta, M.; Skála, T.; Matolínová, I.; Mysliveček, J.; Matolín, V.; Fabris, S., Creating single-atom Pt-ceria catalysts by surface step decoration. *Nat. Commun.* **2016,** *7*, 10801.

[45] Zhang, C.; Michaelides, A.; King, D. A.; Jenkins, S. J., Anchoring Sites for Initial Au Nucleation on CeO_2{111}: O Vacancy versus Ce Vacancy. *J. Phys. Chem. C* **2009,** *113*, 6411-6417.

[46] Fernández, C.; Pezzotta, C.; Raj, G.; Gaigneaux, E. M.; Ruiz, P., Understanding the growth of RuO_2 colloidal nanoparticles over a solid support: An atomic force microscopy study. *Catal. Today* **2016,** *259*, 183-191.

[47] Singh, P.; Hegde, M. S., $Ce_{1-x}Ru_xO_{2-\delta}$ (x=0.05, 0.10): A New High Oxygen Storage Material and Pt, Pd-Free Three-Way Catalyst. *Chem. Mater.* **2009,** *21*, 3337-3345.

[48] Wu, L.; Wiesmann, H. J.; Moodenbaugh, A. R.; Klie, R. F.; Zhu, Y.; Welch, D. O.; Suenaga, M., Oxidation state and lattice expansion of CeO_2 nanoparticles as a function of particle size. *Phys. Rev. B* **2004,** *69*, 125415.

[49] Zhang, F.; Wang, P.; Koberstein, J.; Khalid, S.; Chan, S.-W., Cerium oxidation state in ceria nanoparticles studied with X-ray photoelectron spectroscopy and absorption near edge spectroscopy. *Surf. Sci.* **2004,** *563*, 74-82.

[50] Torbrügge, S.; Reichling, M.; Ishiyama, A.; Morita, S.; Custance, Ó., Evidence of Subsurface Oxygen Vacancy Ordering on Reduced CeO_2(111). *Phys. Rev. Lett.* **2007,** *99*, 056101.

[51] Atanasoska, L.; O'Grady, W. E.; Atanasoski, R. T.; Pollak, F. H., The surface structure of RuO_2: A leed, auger and XPS study of the (110) and (100) faces. *Surf. Sci.* **1988,** *202*, 142-166.

[52] Bhaskar, S.; Dobal, P. S.; Majumder, S. B.; Katiyar, R. S., X-ray photoelectron spectroscopy and micro-Raman analysis of conductive RuO_2 thin films. *J. Appl. Phys.* **2001,** *89*, 2987-2992.

[53] Qadir, K.; Joo, S. H.; Mun, B. S.; Butcher, D. R.; Renzas, J. R.; Aksoy, F.; Liu, Z.; Somorjai, G. A.; Park, J. Y., Intrinsic Relation between Catalytic Activity of CO Oxidation on Ru Nanoparticles and Ru Oxides Uncovered with Ambient Pressure XPS. *Nano Lett.* **2012,** *12*, 5761-5768.

[54] Chan, H. Y. H.; Takoudis, C. G.; Weaver, M. J., High-Pressure Oxidation of Ruthenium as Probed by Surface-Enhanced Raman and X-Ray Photoelectron Spectroscopies. *J. Catal.* **1997,** *172*, 336-345.

[55] Kim, K.; Winograd, N., X-ray photoelectron spectroscopic studies of ruthenium-oxygen surfaces. *J. Catal.* **1974,** *35*, 66-72.

[56] Iembo, A.; Fuso, F.; Arimondo, E.; Ciofi, C.; Pennelli, G.; Curró, G. M.; Neri, F.; Allegrini, M., Pulsed laser deposition and characterization of conductive RuO_2 thin films. *J. Mater. Res.* **2011,** *12*, 1433-1436.

[57] Kurnatowska, M.; Mista, W.; Mazur, P.; Kepinski, L., Nanocrystalline $Ce_{1-x}Ru_xO_2$ – Microstructure, stability and activity in CO and soot oxidation. *Appl. Catal., B* **2014,** *148-149*, 123-135.

[58] Bolzan, A. A.; Fong, C.; Kennedy, B. J.; Howard, C. J., Structural Studies of Rutile-Type Metal Dioxides. *Acta Crystallogr. B* **1997,** *53*, 373-380.

[59] Sharma, S.; Hu, Z.; Zhang, P.; McFarland, E. W.; Metiu, H., CO_2 methanation on Ru-doped ceria. *J. Catal.* **2011,** *278*, 297-309.

[60] Shinde, V. M.; Madras, G., Synthesis of nanosized $Ce_{0.85}M_{0.1}Ru_{0.05}O_{2-\delta}$ (M=Si, Fe) solid solution exhibiting high CO oxidation and water gas shift activity. *Appl. Catal., B* **2013,** *138-139*, 51-61.

[61] Wang, C.; Liu, S.; Wang, D.; Chen, Q., Interface engineering of Ru–Co_3O_4 nanocomposites for enhancing CO oxidation. *J. Mater. Chem. A* **2018,** *6*, 11037-11043.

[62] Liu, Z.; Zhang, F.; Rui, N.; Li, X.; Lin, L.; Betancourt, L. E.; Su, D.; Xu, W.; Cen, J.; Attenkofer, K.; Idriss, H.; Rodriguez, J. A.; Senanayake, S. D., Highly Active Ceria-Supported Ru Catalyst for the Dry Reforming of Methane: In Situ Identification of $Ru^{\delta+}$–Ce^{3+} Interactions for Enhanced Conversion. *ACS Catal.* **2019,** *9*, 3349-3359.

[63] Paparazzo, E.; Ingo, G. M.; Zacchetti, N., X-ray induced reduction effects at CeO_2 surfaces: An X-ray photoelectron spectroscopy study. *J. Vac. Sci. Technol.* **1991,** *9*, 1416-1420.

[64] Pu, Z.-Y.; Liu, X.-S.; Jia, A.-P.; Xie, Y.-L.; Lu, J.-Q.; Luo, M.-F., Enhanced Activity for CO Oxidation over Pr- and Cu-Doped CeO_2 Catalysts: Effect of Oxygen Vacancies. *J. Phys. Chem. C* **2008,** *112*, 15045-15051.

[65] Widmann, D.; Leppelt, R.; Behm, R. J., Activation of a Au/CeO_2 catalyst for the CO oxidation reaction by surface oxygen removal/oxygen vacancy formation. *J. Catal.* **2007,** *251*, 437-442.

[66] Liotta, L. F.; Ousmane, M.; Di Carlo, G.; Pantaleo, G.; Deganello, G.; Marcì, G.; Retailleau, L.; Giroir-Fendler, A., Total oxidation of propene at low temperature over Co_3O_4–CeO_2 mixed oxides: Role of surface oxygen vacancies and bulk oxygen mobility in the catalytic activity. *Appl. Catal., A* **2008,** *347*, 81-88.

[67] Kim, H. Y.; Lee, H. M.; Henkelman, G., CO Oxidation Mechanism on CeO_2-Supported Au Nanoparticles. *J. Am. Chem. Soc.* **2012,** *134*, 1560-1570.

[68] Mo, Y.; Antonio, M. R.; Scherson, D. A., In Situ Ru K-Edge X-Ray Absorption Fine Structure Studies of Electroprecipitated Ruthenium Dioxide Films with Relevance to Supercapacitor Applications. *J. Phys. Chem. B* **2000,** *104*, 9777-9779.

[69] McKeown, D. A.; Hagans, P. L.; Carette, L. P. L.; Russell, A. E.; Swider, K. E.; Rolison, D. R., Structure of Hydrous Ruthenium Oxides: Implications for Charge Storage. *J. Phys. Chem. B* **1999,** *103*, 4825-4832.

[70] Ravel, B.; Newville, M., ATHENA, ARTEMIS, HEPHAESTUS: data analysis for X-ray absorption spectroscopy using IFEFFIT. *J. Synchrotron Radiat.* **2005,** *12*, 537-541.

[71] Lykaki, M.; Pachatouridou, E.; Carabineiro, S. A. C.; Iliopoulou, E.; Andriopoulou, C.; Kallithrakas-Kontos, N.; Boghosian, S.; Konsolakis, M., Ceria nanoparticles shape effects on the structural defects and surface chemistry: Implications in CO oxidation by Cu/CeO_2 catalysts. *Appl. Catal., B* **2018,** *230*, 18-28.

[72] Zhou, K.; Wang, X.; Sun, X.; Peng, Q.; Li, Y., Enhanced catalytic activity of ceria nanorods from well-defined reactive crystal planes. *J. Catal.* **2005,** *229*, 206-212.

[73] Hu, Z.; Liu, X.; Meng, D.; Guo, Y.; Guo, Y.; Lu, G., Effect of Ceria Crystal Plane on the Physicochemical and Catalytic Properties of Pd/Ceria for CO and Propane Oxidation. *ACS Catal.* **2016,** *6*, 2265-2279.

[74] Trovarelli, A., Catalytic Properties of Ceria and CeO_2-Containing Materials. *Catal. Rev.* **1996,** *38*, 439-520.

[75] Wu, Z.; Cheng, Y.; Tao, F.; Daemen, L.; Foo, G. S.; Nguyen, L.; Zhang, X.; Beste, A.; Ramirez-Cuesta, A. J., Direct Neutron Spectroscopy Observation of Cerium Hydride Species on a Cerium Oxide Catalyst. *J. Am. Chem. Soc.* **2017,** *139*, 9721-9727.

[76] Yang, C.; Yu, X.; Heißler, S.; Nefedov, A.; Colussi, S.; Llorca, J.; Trovarelli, A.; Wang, Y.; Wöll, C., Surface Faceting and Reconstruction of Ceria Nanoparticles. *Angew. Chem. Int. Ed.* **2017,** *56*, 375-379.

[77] Soler, L.; Casanovas, A.; Urrich, A.; Angurell, I.; Llorca, J., CO oxidation and $COPrO_x$ over preformed Au nanoparticles supported over nanoshaped CeO_2. *Appl. Catal., B* **2016,** *197*, 47-55.

[78] Spezzati, G.; Benavidez, A.; DeLaRiva, A. T.; Su, Y.; Hofmann, J. P.; Asahina, S.; Olivier, E. J.; Neethling, J. H.; Miller, J. T.; Datye, A. K.; Hensen, E. J. M., CO oxidation by Pd supported on CeO_2(100) and CeO_2(111) facets. *Appl. Catal., B* **2018,** *243*, 36-46.

[79] Assmann, J.; Narkhede, V.; Khodeir, L.; Löffler, E.; Hinrichsen, O.; Birkner, A.; Over, H.; Muhler, M., On the Nature of the Active State of Supported Ruthenium Catalysts Used for the Oxidation of Carbon Monoxide: Steady-State and Transient Kinetics Combined with in Situ Infrared Spectroscopy. *J. Phys. Chem. B* **2004,** *108*, 14634-14642.

[80] Aßmann, J.; Löffler, E.; Birkner, A.; Muhler, M., Ruthenium as oxidation catalyst: bridging the pressure and material gaps between ideal and real systems in heterogeneous catalysis by applying DRIFT spectroscopy and the TAP reactor. *Catal. Today* **2003,** *85*, 235-249.

[81] Kantcheva, M.; Sayan, S., On the mechanism of CO adsorption on a silica - supported ruthenium catalyst. *Catal. Lett.* **1999,** *60*, 27-38.

[82] Yokomizo, G. H.; Louis, C.; Bell, A. T., An infrared study of CO adsorption on reduced and oxidized Ru/SiO_2. *J. Catal.* **1989,** *120*, 1-14.

[83] Derk, A. R.; Moore, G. M.; Sharma, S.; McFarland, E. W.; Metiu, H., Catalytic Dry Reforming of Methane on Ruthenium-Doped Ceria and Ruthenium Supported on Ceria. *Top. Catal.* **2014,** *57*, 118-124.

[84] Peden, C. H. F.; Goodman, D. W.; Weisel, M. D.; Hoffmann, F. M., In-situ FT-IRAS study of the CO oxidation reaction over Ru(001): I. Evidence for an Eley-Rideal mechanism at high pressures? *Surf. Sci.* **1991,** *253*, 44-58.

[85] Chin, S. Y.; Williams, C. T.; Amiridis, M. D., FTIR Studies of CO Adsorption on Al_2O_3- and SiO_2-Supported Ru Catalysts. *J. Phys. Chem. B* **2006,** *110*, 871-882.

[86] Chen, H.-T., First-Principles Study of CO Adsorption and Oxidation on Ru-Doped CeO_2(111) Surface. *J. Phys. Chem. C* **2012,** *116*, 6239-6246.

[87] Nie, L.; Mei, D.; Xiong, H.; Peng, B.; Ren, Z.; Hernandez, X. I. P.; DeLaRiva, A.; Wang, M.; Engelhard, M. H.; Kovarik, L.; Datye, A. K.; Wang, Y., Activation of surface lattice oxygen in single-atom Pt/CeO_2 for low-temperature CO oxidation. *Science* **2017,** *358*, 1419.

[88] Hosokawa, S., State of Ru on CeO_2 and its catalytic activity in the wet oxidation of acetic acid. *Appl. Catal., B* **2003,** *45*, 181-187.

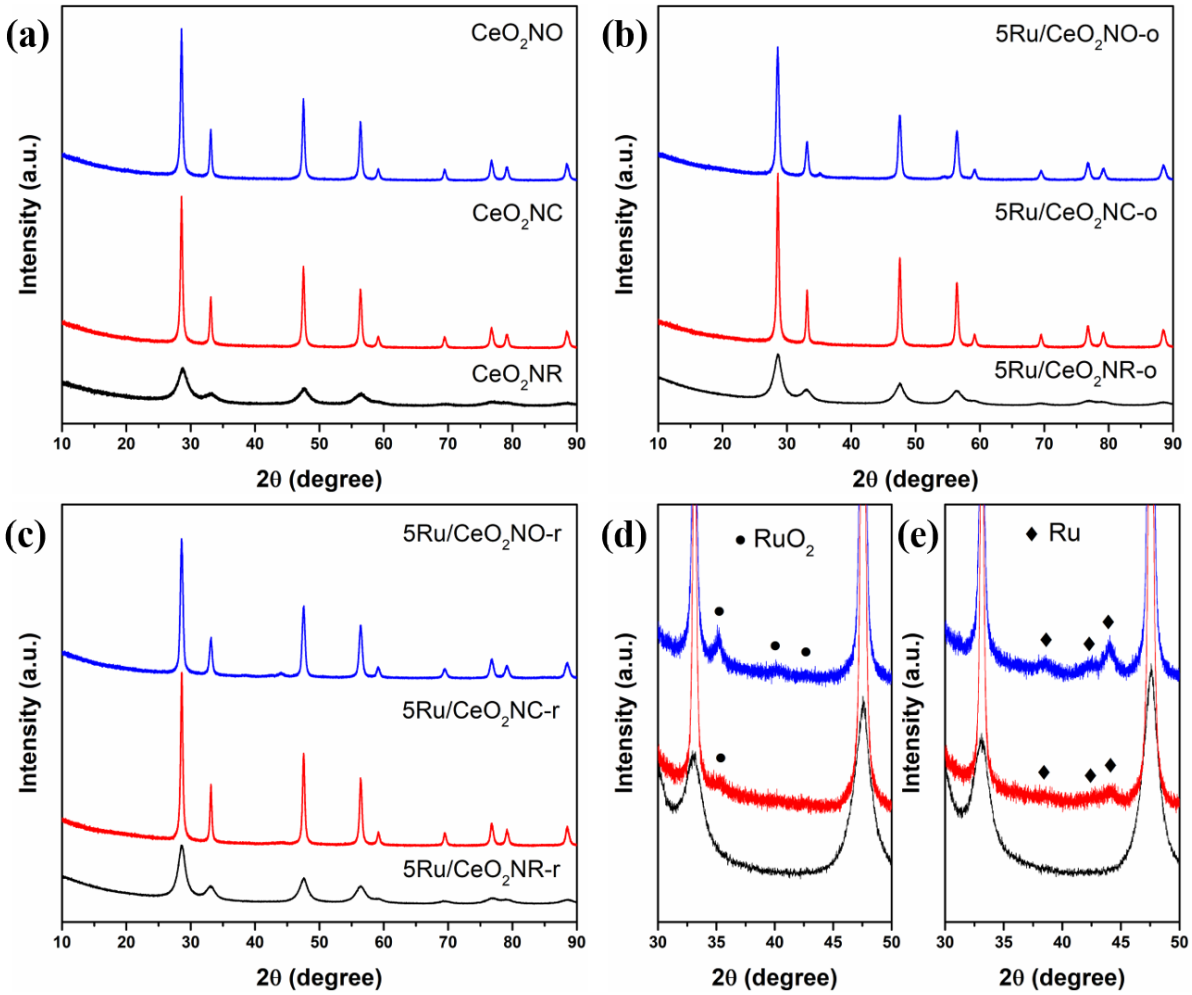

Figure 1 XRD patterns of (a) CeO_2 supports and different shaped 5.0 wt% Ru/CeO_2 catalysts after (b) oxidation and (c) reduction treatment. Expanded regions (d and e) showing reflections of RuO_2 and Ru peaks between 30° and 50°.

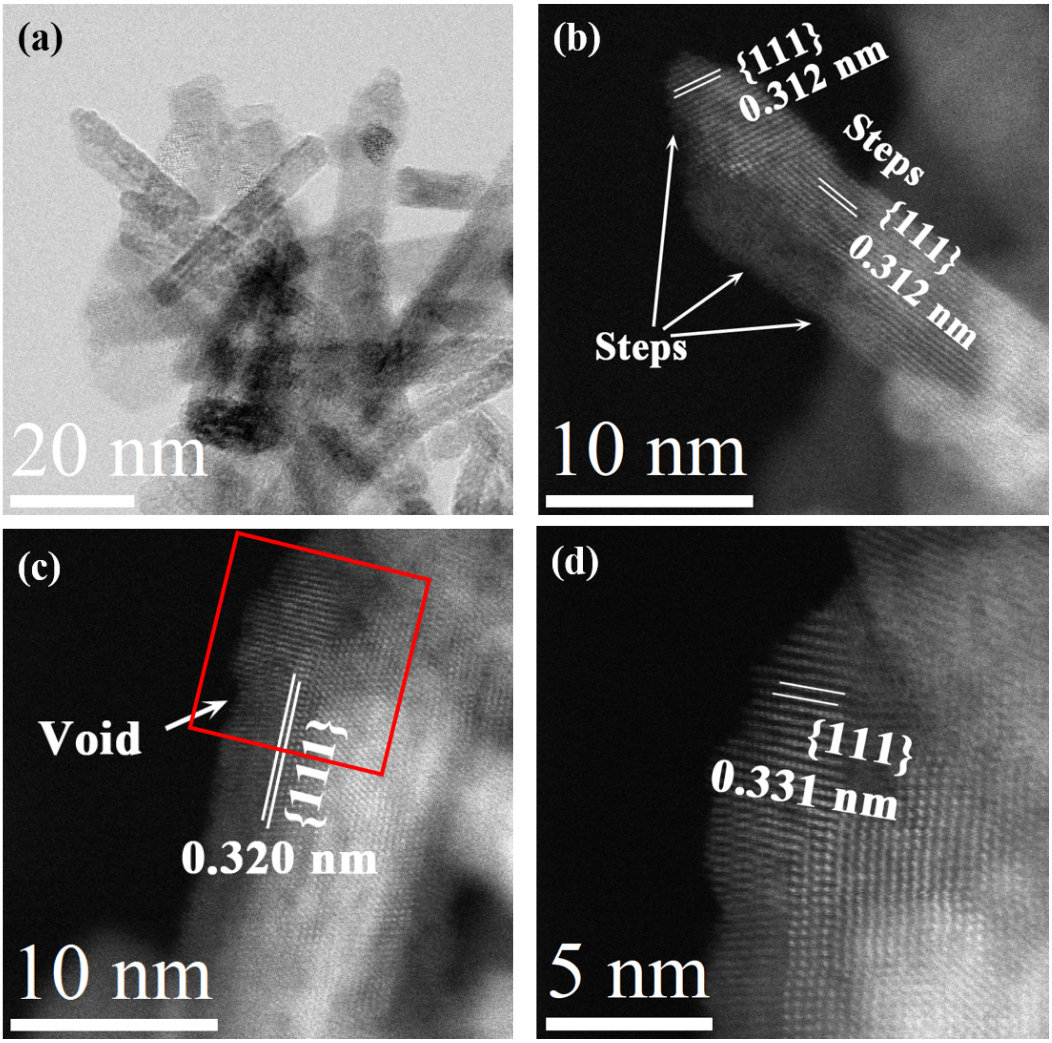

Figure 2 (a) Typical low-magnification TEM image and (b-d) HAADF-STEM images of 5.0 wt% Ru/CeO_2NR catalyst after reduction treatment; (d) is the enlarged HAADF-STEM image of the red square section shown in (c).

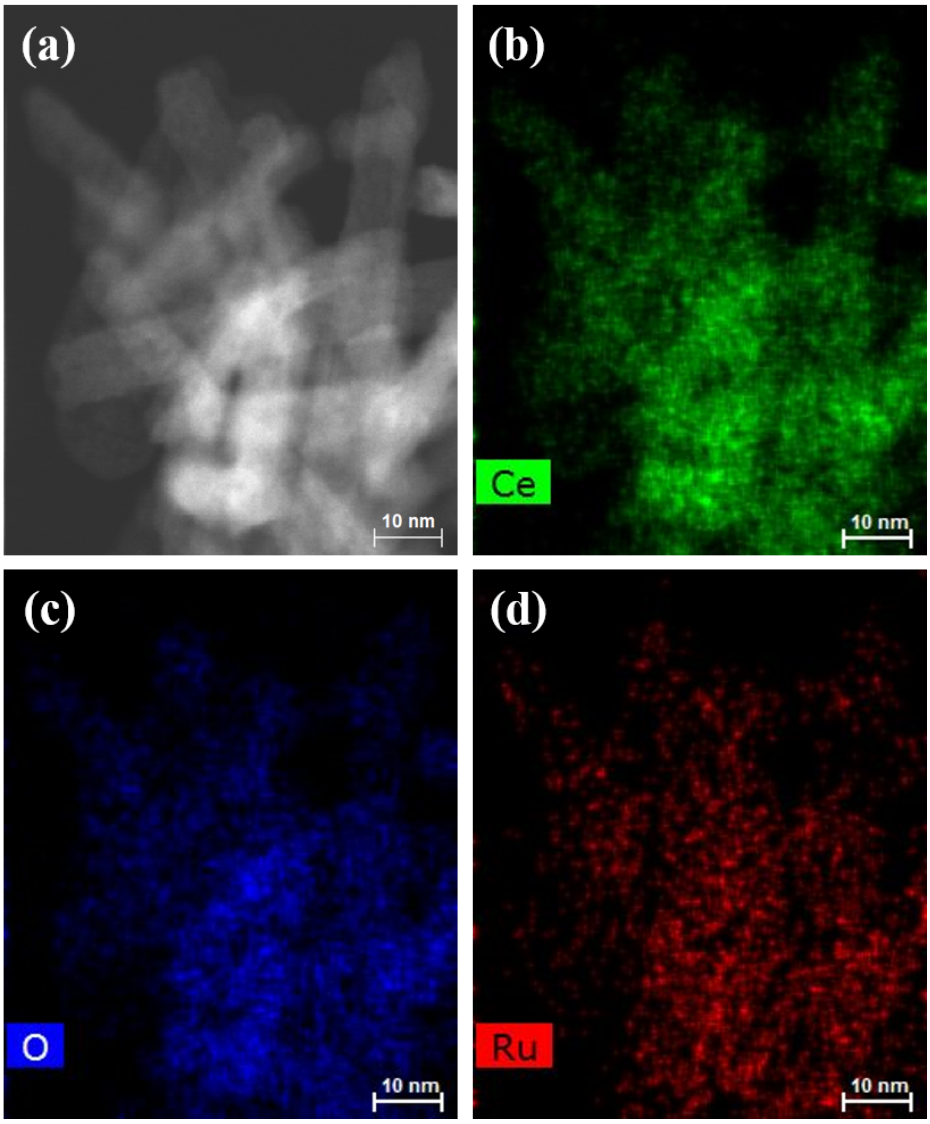

Figure 3 (a) HAADF-STEM image and STEM-EDS elemental mappings of (b) Ce; (c) O and (d) Ru for 5.0 wt% Ru/CeO_2NR catalyst after reduction treatment.

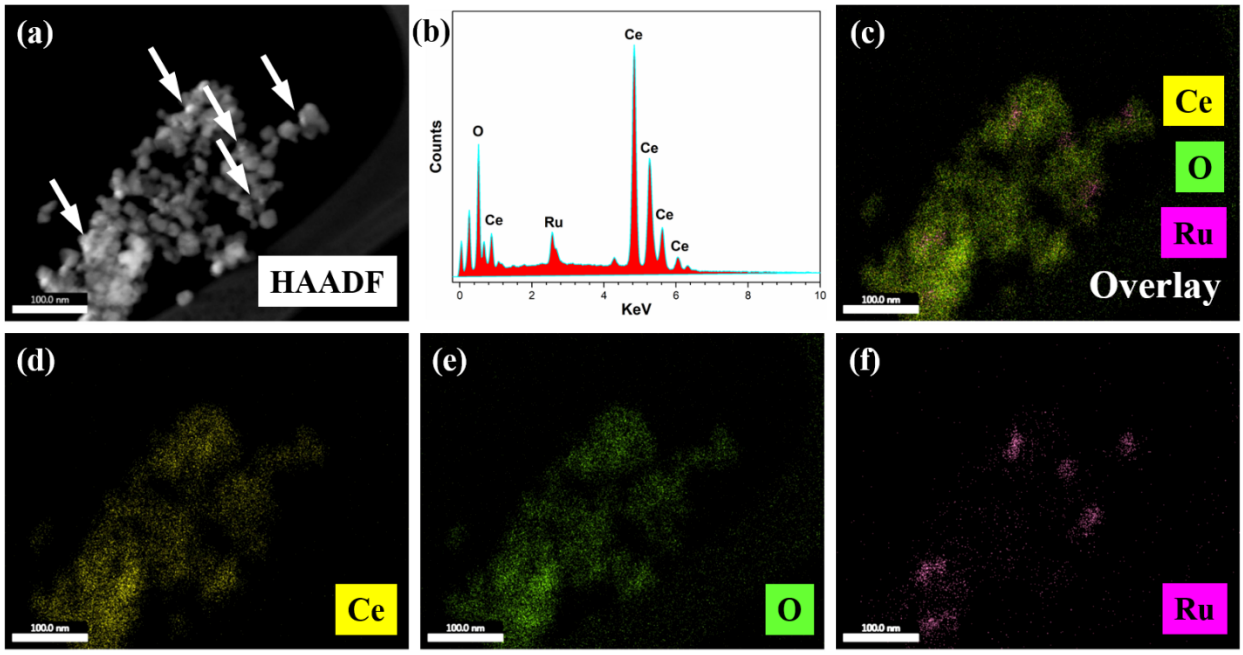

Figure 4 (a) HAADF image of 5.0 wt% Ru/CeO_2NO catalyst after reduction treatment; (b) EDS spectrum and chemical composition analysis; EDS mapping of (c) Ce + O + Ru overlay, (d) Ce, (e) O, and (f) Ru elements of the area where (a) was obtained.

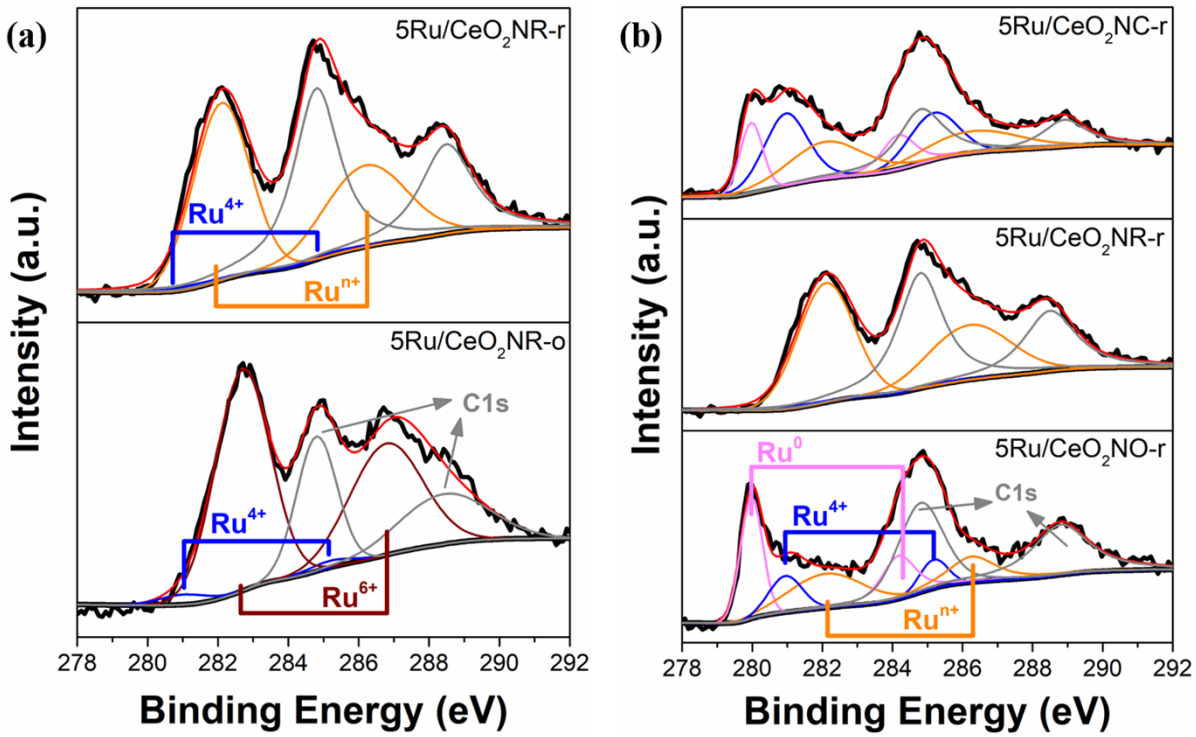

Figure 5 Deconvolution of XPS of Ru 3d for (a) 5.0 wt% Ru/CeO_2NR catalyst after oxidation and reduction treatment; (b) different shaped 5.0 wt% Ru/CeO_2 catalysts after reduction treatment.

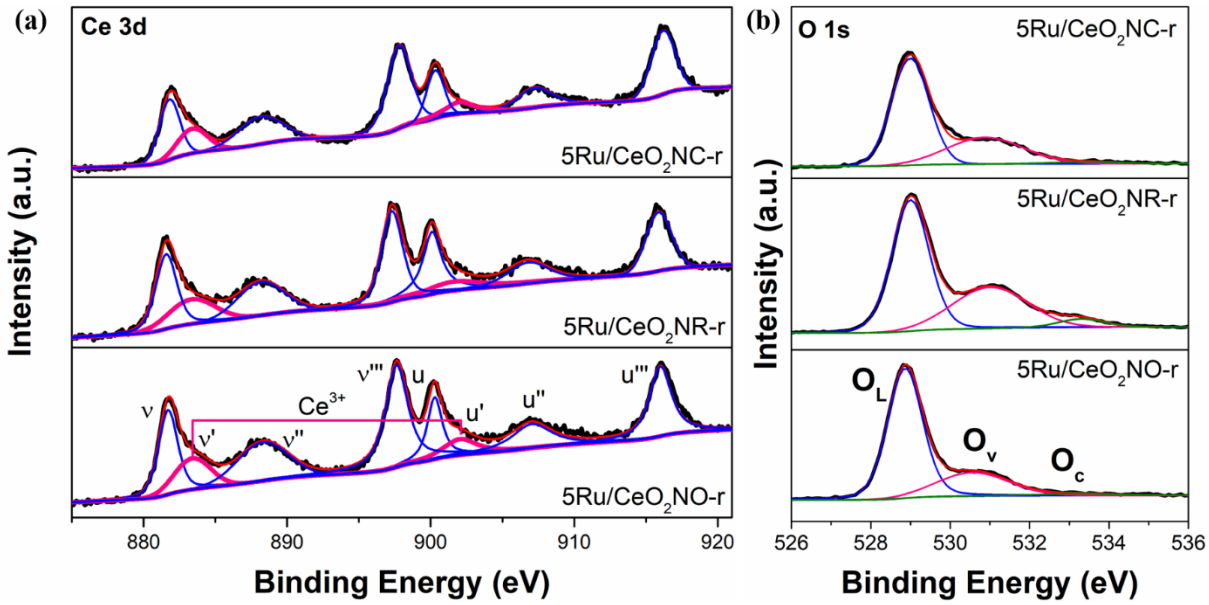

Figure 6 Deconvolution of XPS of (a) Ce 3d and (b) O 1s for different shaped 5.0 wt% Ru/CeO_2 catalysts after reduction treatment.

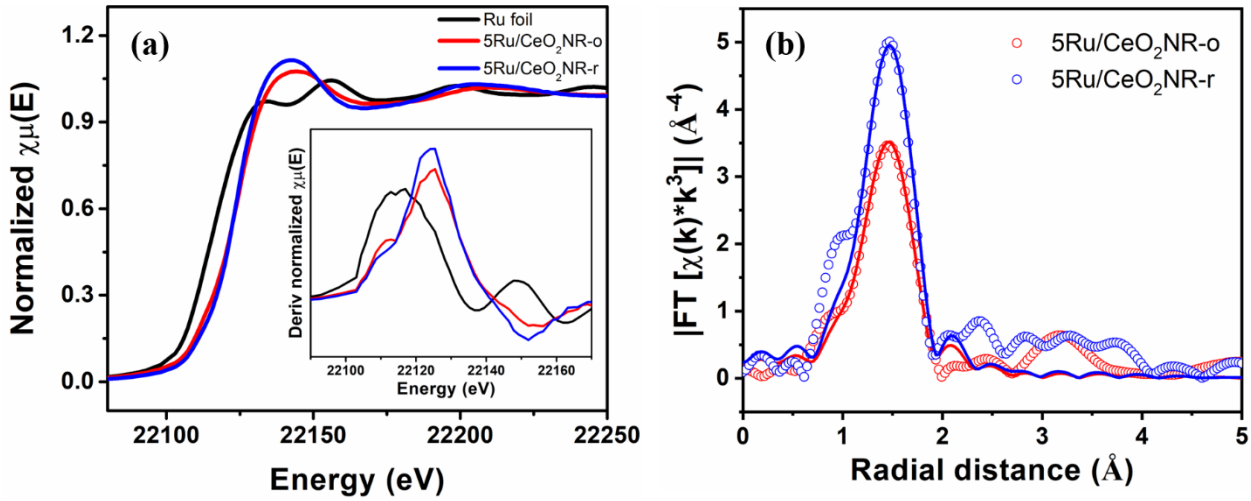

Figure 7 (a) The comparison of Ru K-edge XANES spectra of Ru foil and 5.0 wt% Ru/CeO_2NR catalysts after oxidation and reduction treatment (Inset: first derivative spectra of the XANES data); (b) The comparison of EXAFS spectra (open dot) and the best fit (solid lines) of the 5.0 wt% Ru/CeO_2NR catalysts after oxidation and reduction treatment.

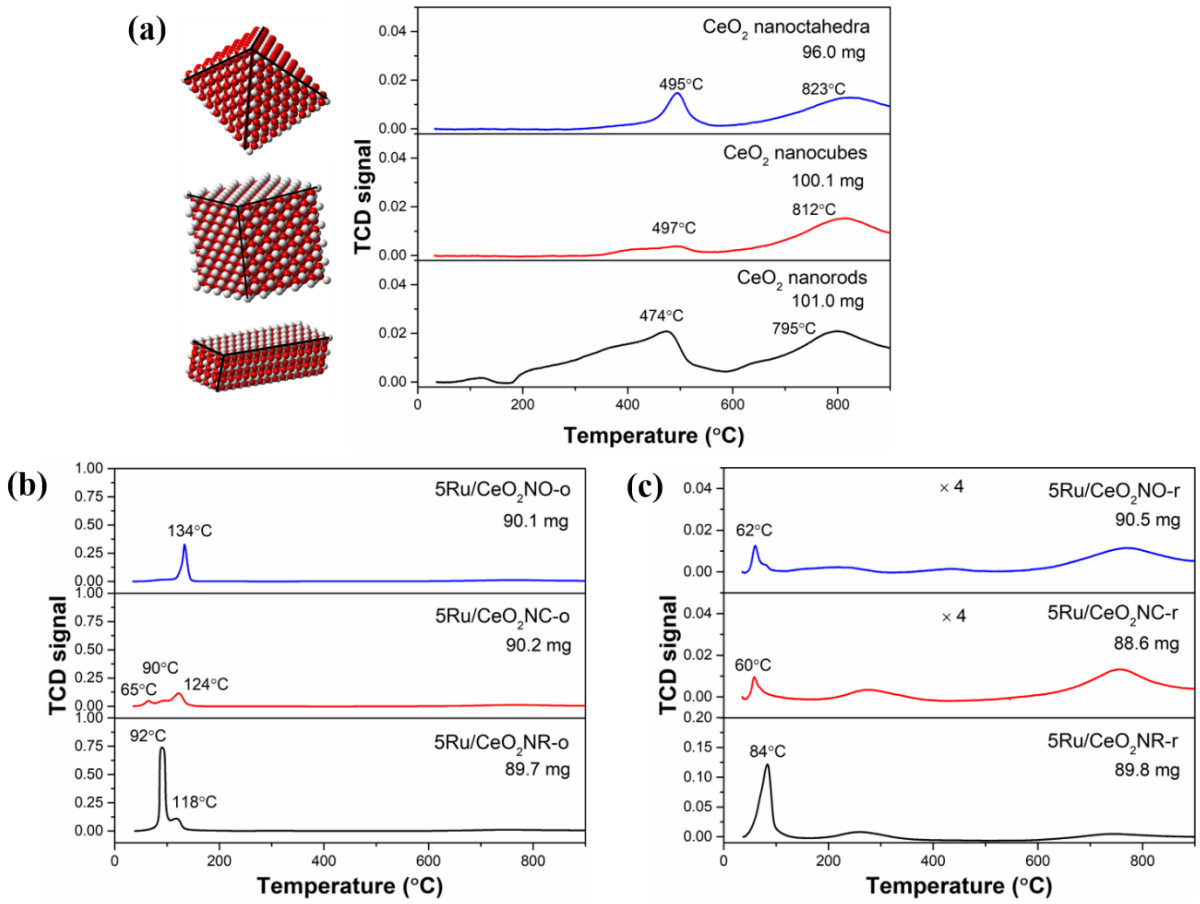

Figure 8 (a) Crystal structure models and H_2-TPR profiles of CeO_2 NO, NC and NR; different shaped 5.0 wt% Ru/CeO_2 catalysts (b) after oxidation and (c) after reduction treatment.

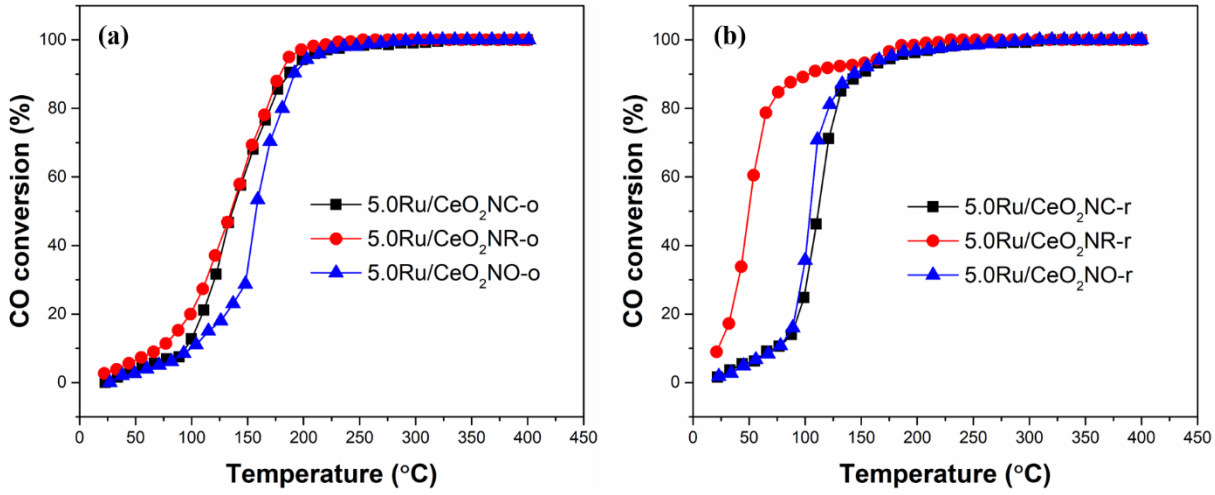

Figure 9 CO conversion curves of different shaped 5.0 wt% Ru/CeO_2 catalysts (a) after oxidation and (b) after reduction treatment.

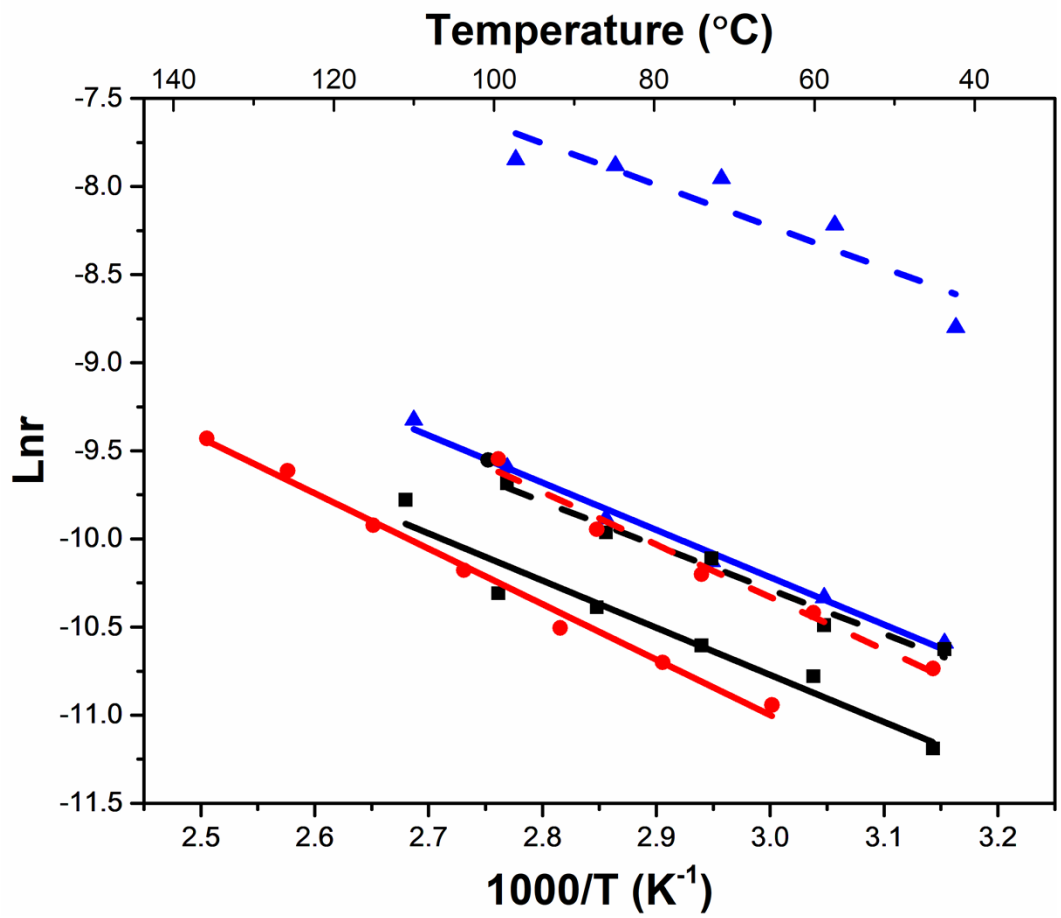

Figure 10 Arrhenius plots of lnr versus 1/T for different shaped 5.0 wt% Ru/CeO_2 catalysts. (solid line: oxidation treatment; dash line: reduction treatment; ■: CeO_2 NC support; ●: CeO_2 NO support; ▲: CeO_2 NR support.

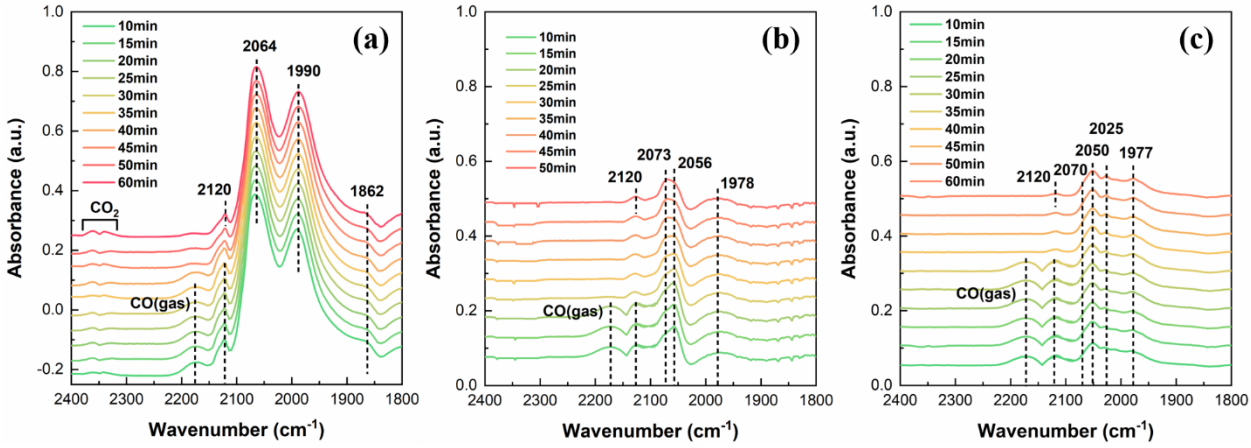

Figure 11 Time-dependent in-situ DRIFTS spectra of CO adsorption on different shaped 5.0 wt% Ru/CeO_2 catalysts after reduction treatment: (a) $5Ru/CeO_2$NR-r, (b) $5Ru/CeO_2$NC-r, (c) $5Ru/CeO_2$NO-r.

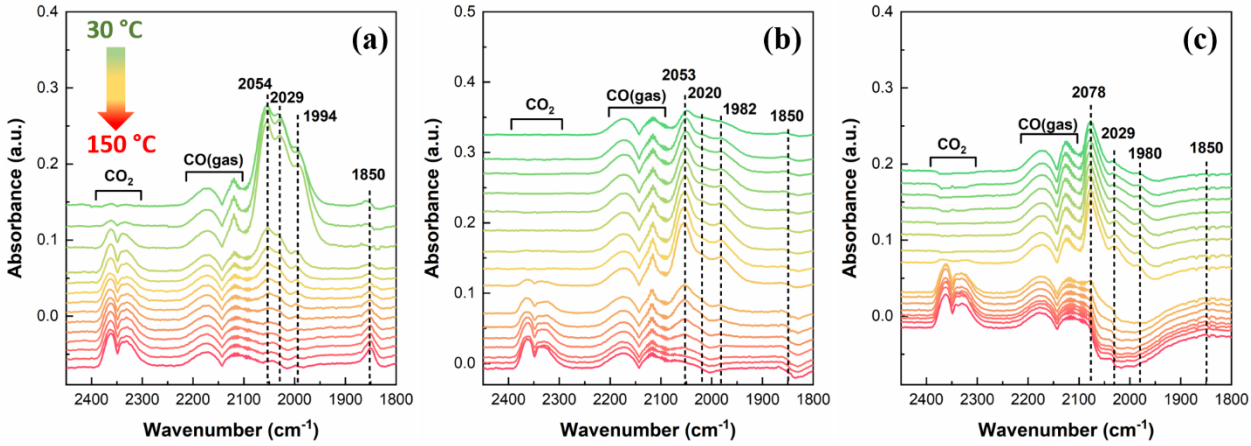

Figure 12 Temperature-dependent in-situ DRIFTS spectra of CO oxidation on different shaped 5.0 wt% Ru/CeO_2 catalysts after reduction treatment: (a) 5Ru/CeO_2NR-r, (b) 5Ru/CeO_2NC-r, (c) 5Ru/CeO_2NO-r.

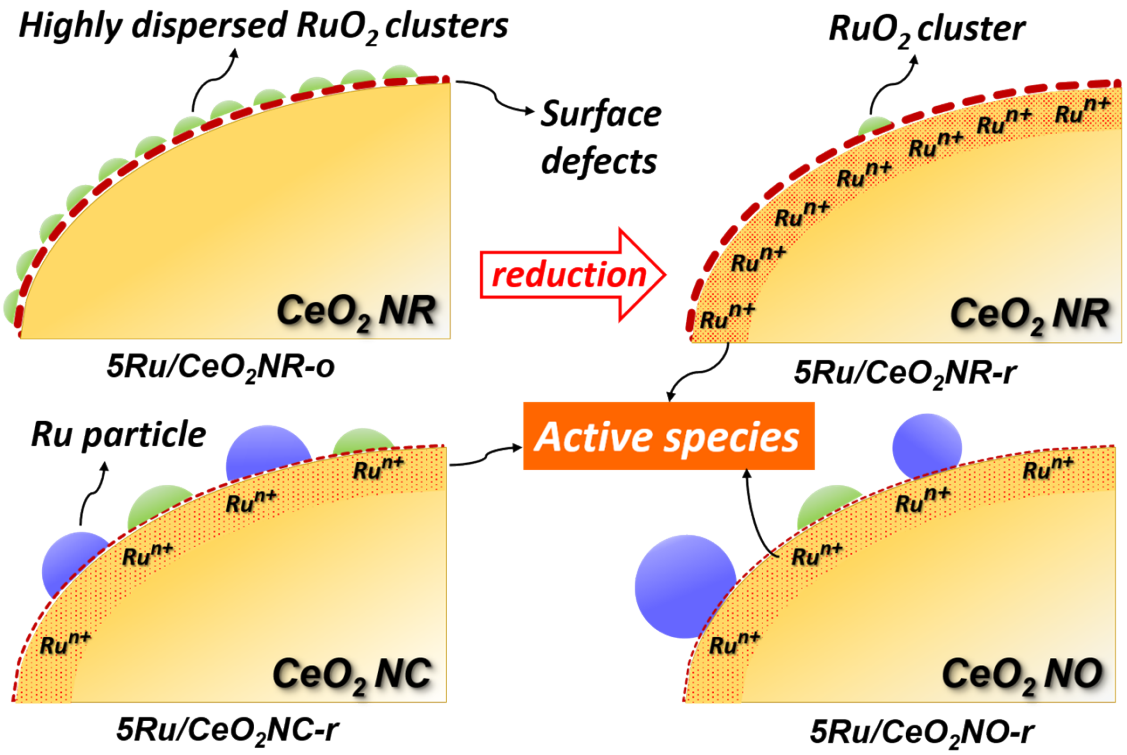

Figure 13 Schematic diagram of the interactions between ruthenium species and different shaped CeO_2 supports.

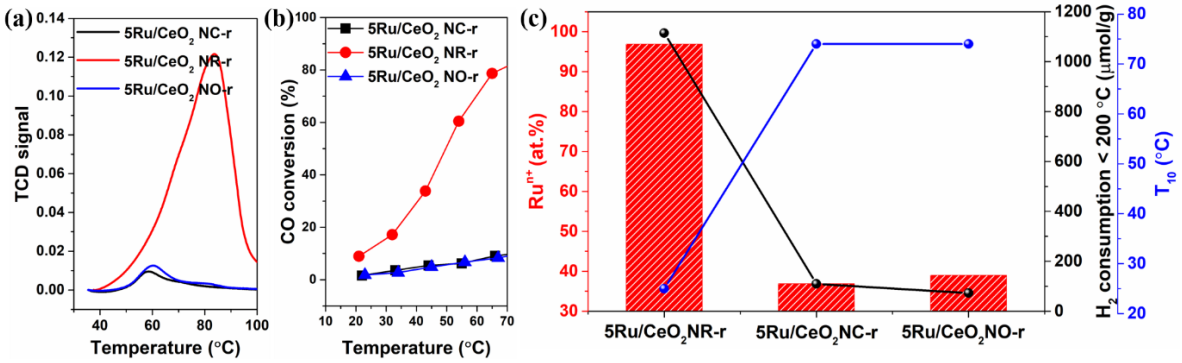

Figure 14 (a) H_2-TPR performance (<100 °C) and (b) low-temperature CO oxidation of different shaped 5.0 wt% Ru/CeO_2 catalysts after reduction treatment; (c) Relationship between the H_2 consumption below 200 °C and 10%-conversion temperature (T_{10}) and the amount of Ru^{n+} species on different shaped 5.0 wt% Ru/CeO_2 catalysts after reduction treatment.

Table 1 Average crystallite size measured using CeO_2 (111) peak, BET surface area, T_{10}, T_{50} and the activation energy of CeO_2 NO, NC, NR and different shaped 5.0 wt% Ru/CeO_2 catalysts after oxidation and after reduction treatment.

Sample	Crystallite size of CeO_2 (nm)	BET surface area (m^2/g)	T_{10} (°C)	T_{50} (°C)	E_a (kJ/mol)
CeO_2 NO	16.6	45.9	-	-	-
CeO_2 NC	22.8	48.7	-	-	-
CeO_2 NR	4.5	105.5	-	-	-
5Ru/CeO_2 NO-o	17.7	33.8	99	157	26.1
5Ru/CeO_2 NC-o	22.7	45.1	96	135	22.2
5Ru/CeO_2 NR-o	5.2	108.4	71	135	22.3
5Ru/CeO_2 NO-r	18.2	38.8	74	104	24.8
5Ru/CeO_2 NC-r	22.5	48.1	74	112	20.8
5Ru/CeO_2 NR-r	5.6	107.4	25	50	19.6

Table 2 XPS data of various samples.

Sample	Ru^0 (at.%)	Ru^{4+} (at.%)	Ru^{n+} (at.%)	O_V/O_L	Ce^{3+} (at.%)
5Ru/CeO_2 NR-r	0	3.1	96.9	0.59	16.0
5Ru/CeO_2 NC-r	21.7	41.4	36.9	0.50	13.4
5Ru/CeO_2 NO-r	42.1	18.9	39.0	0.34	13.5

Table 3 Redox characteristics of ceria supports.

Sample	H_2 consumption (μmol H_2 g^{-1})			O_s/O_b ratio	Peak temperature (°C)	
	O_s peak	O_b peak	Total		O_s peak	O_b peak
CeO_2 NO	310.2	728.8	1039.0	0.43	495	823
CeO_2 NC	134.0	867.5	1001.5	0.15	497	812
CeO_2 NR	1396.8	1305.5	2702.3	1.07	474	795

Table 4 H_2 consumption and oxygen contents of different shaped 5.0 wt% Ru/CeO_2 samples after oxidation and reduction treatment based on H_2-TPR result.

Sample	**H_2 consumption (μmol/g)**				**Theor. H_2 consumption $RuO_2 \rightarrow Ru$ (μmol/g)**	**Oxygen content**
	Up to 200 °C	200-500 °C	500-900 °C	Total		
$5Ru/CeO_2$ NR-o	3511.2	61.2	555.9	4128.3	989.4	$CeO_{1.43*}$
$5Ru/CeO_2$ NC-o	1354.4	40.2	711.5	2106.1	989.4	$CeO_{1.80}$
$5Ru/CeO_2$ NO-o	1297.3	67.6	638.5	2003.4	989.4	$CeO_{1.84}$
$5Ru/CeO_2$ NR-r	1114.5	427.6	599.5	2141.6	0	$CeO_{1.61*}$
$5Ru/CeO_2$ NC-r	109.7	167.9	753.1	1030.7	0	$CeO_{1.81}$
$5Ru/CeO_2$ NO-r	72.9	141.7	621.3	835.9	0	$CeO_{1.85}$

*See the explanation in the text for these low oxygen concentration values in CeO_x.

Table 5 Assignment of the bands observed after adsorption of CO on different shaped 5.0 wt% Ru/CeO_2 catalysts after reduction treatment.

This work (cm^{-1})	References	Assignment
~2120/~2064, ~2120/~2070	[79-82]	$Ru^{\delta+}$-$(CO)_x$
~1990	[79, 80]/[83]	CO adsorbed on oxygen vacancies/CO IR-adsorption band unique to ruthenium-doped ceria
~2025, ~2050	[84, 85]	Ru^0-CO
~1980	[86]	bridged CO (bonded to Ru at the Ru-CeO_2 interface)

Graphic Abstract